Study on the structural characteristics, in vitro hypoglycemic activity, and regulatory mechanisms of *Alpinia oxyphylla* polysaccharide in modulating human gut microbiota

Junlin Wu[1], Jiayue Li[1], Fengchuan Ma[1], Sijie Huang[1], Xincheng Ye[1], Minghui Yang[1], Hua Yang[1], Yunping Peng[2]*, Siming Zhu[1,3,4]*, Meng Wang[1,3]*

[1]School of Food Science and Engineering, Guangdong Ocean University, Yangjiang, China; [2]Guangzhou Wondfo Health Science and Technology Co., Ltd., Guangzhou, China; [3]School of Life and Geographic Sciences, Kashgar University, Kashi, Xinjiang, China; [4]School of Food Science and Technology, South China University of Technology, 381 Wushan Road, Tianhe District, Guangzhou, China

***Corresponding Authors:** Meng Wang, School of Food Science and Engineering, Guangdong Ocean University, Yangjiang, and School of Life and Geographic Sciences, Kashgar University, Kashi, Xinjiang, China. Email: caspianwm@163.com; Yunping Peng, Guangzhou Wondfo Health Science and Technology Co., Ltd., Guangzhou, China. Email: pypcn@163.com; Siming Zhu, School of Food Science and Engineering, Guangdong Ocean University, Yangjiang, China; School of Food Science and Technology, South China University of Technology, 381 Wushan Road, Tianhe District, Guangzhou, China School of Life and Geographic Sciences, Kashgar University, Kashi, Xinjiang, China. Email: lfsmzhu@scut.edu.cn

Academic Editor: Prof. Bernard Fioretti – University of Perugia, Italy

Received: 23 October 2025; Accepted: 12 January 2026; Published: 1 April 2026

ORIGINAL ARTICLE

Abstract

This study aimed to systematically compare the structural characteristics, in vitro hypoglycemic activity, and regulatory effects on gut microbiota of *Alpinia oxyphylla* polysaccharides (AOFP) obtained by three extraction techniques, high-pressure and high-temperature (HH), acid-assisted high-pressure and high-temperature (AHP), and *Aspergillus niger* fermentation (ANF), to elucidate their structure–activity relationship and gut microbiota regulation mechanisms. By comparing the three types of AOFP (AOFP-HH, AOFP-AHP, AOFP-ANF), we revealed intrinsic associations among structure, activity, and microbiota regulation. The HH method promoted the ordered arrangement of β-1,3-glucan chains, forming a semicrystalline state and folded lamellar structures, thereby exhibiting the strongest hypoglycemic activity (α-amylase inhibition rate: 97.08 %; α-glucosidase inhibition rate: 59.43 %). The key mechanism lies in the synergy between the integrity of β-1,3-glycosidic bonds and the galacturonic acid content (11.74 %); together, they enhance activity through spatial hindrance effects and hydrogen bond networks. On the other hand, the AHP method, due to acid-induced cleavage of glycosidic bonds, generated amorphous low-molecular-weight structures (1.03 kDa), leading to a marked reduction in activity. The ANF method produced medium-molecular-weight fragments (1.14 kDa) via enzymatic hydrolysis. In terms of gut microbiota regulation, all AOFPs significantly promoted early butyrate production; notably, the HH group maintained a butyrate concentration of 0.076 mmol/L at 48 h. Each polysaccharide sample specifically increased the *Firmicutes* and stimulated the proliferation of *Ligilactobacillus*, thereby improving intestinal barrier function. Interestingly, the ANF group uniquely upregulated the abundance of *Fusobacteriota*, suggesting potential immunomodulatory capacity. Further analysis indicated that different processing techniques modulate selective microbial metabolic pathways through conformational differences. The AOFP-HH prepared by the HH method combines high hypoglycemic activity with structural stability, making it an ideal functional food additive.

Meanwhile, the distinctive microbiota interaction mechanism exhibited by the ANF method offers novel insights for the development of personalized probiotics. In conclusion, our findings lay a solid theoretical foundation for the precise design of *A. oxyphylla* polysaccharides and their application in the prevention and treatment of metabolic diseases.

Keywords: *Alpinia oxyphylla*; intestinal microbiota ; polysaccharide ; structural analysis

Introduction

Alpinia oxyphylla is a perennial herb of the genus *Alpinia* (family Zingiberaceae), growing 1–3 m tall, with lanceolate leaves, paniculate inflorescences, and ellipsoid fruits containing multiple seeds (Li *et al*., 2020; Zhang *et al*., 2018). It is native to Hainan Province, China, and mainly distributed in tropical and subtropical regions, including southern China, South Korea, and Japan (Huang *et al*., 2019; Park *et al*., 2022). Recognized as one of China's traditional "Four Great South Medicinal Herbs" and recorded in the Compendium of Materia Medica (Ben Cao Gang Mu), *A. oxyphylla* has a medicinal history of more than 2000 years. Its dried fruits are usually processed by soaking in brine and light stir-frying before being used in traditional medicine for "warming the spleen to relieve diarrhea, controlling saliva, and warming the kidneys to secure essence," mainly treating salivation, gastric pain, diarrhea, and kidney deficiency (Li *et al*., 2024).

Modern pharmacological studies have shown that *A. oxyphylla* exhibits a wide range of biological activities. Key compounds such as diarylheptanoids and sesquiterpenoids can inhibit BACE1 activity and reverse Aβ-induced neuronal damage, and help ameliorate diabetes, according to Ge *et al*. (2024). These components also enhance macrophage phagocytic rates as reported by Yang *et al*. (2020), and exert antiproliferative and proapoptotic effects on HepG2 cells through ROS-mediated pathways, as demonstrated in Zhang *et al*. (2015). These findings suggest the plant holds potential for anti-liver fibrosis, anticancer, and antidiabetic applications.

The bioactivity of natural plant polysaccharides depends strongly on their chemical structures, particularly monosaccharide composition and glycosidic bond configuration, as noted by Borjigin *et al*. (2023) and Ruan *et al*. (2021). *A. oxyphylla* fruit polysaccharides (AOFPs) are important bioactive components, and their structural–functional relationship is now a major research focus. Different extraction methods significantly influence AOFP properties. Conventional hot water extraction produces high-molecular-weight heterogeneous polysaccharides. For example, Zhang *et al*. (2015) obtained polysaccharides with a molecular weight of around 2.2 kDa, primarily composed of glucose and galactose. While this method gives high yields, it often results in mixtures of active components. Ultrasound-assisted extraction uses cavitation to break cell walls, yielding lower-molecular-weight fragments of about 1.5 kDa. These fragments exhibit approximately 15% higher α-glucosidase inhibitory activity than hot water extracts, according to Li *et al*. (2020). Microwave-assisted extraction rapidly heats samples to release polysaccharides rich in arabinogalactan, constituting over 60% of the product. These extracts promote higher macrophage phagocytosis, as shown by Yang *et al*. (2020).

In addition to hypoglycemic potential, AOFP demonstrates significant antioxidant activity according to Ruan *et al*. (2021), immunomodulatory effects, such as promoting splenic lymphocyte proliferation by 28%, and anti-inflammatory properties as reported by Zhang *et al*. (2015). However, current studies only characterize polysaccharides from a single extraction method and correlate them with individual activity indicators. There is a lack of systematic comparison and integrated evidence that connect the multidimensional structural features of AOFPs from different extraction processes with their comprehensive bioactivities. Therefore, this study aims to systematically compare three AOFP extraction techniques: high-pressure and high-temperature (HH), acid-assisted high-pressure and high-temperature (AHP), and *Aspergillus niger* fermentation (ANF). The comparison focuses on key physicochemical properties, including extraction yield, purity, molecular weight distribution, monosaccharide composition, and surface morphology.

Based on these physicochemical analyses, we further evaluated the in vitro inhibitory effects of different AOFPs on α-amylase and α-glucosidase, and investigated their regulatory effects on gut microbiota composition and related metabolites. This study clarifies the structure–activity relationships among extraction methods, polysaccharide structural features, hypoglycemic efficacy, and microbiota regulation. These findings provide

a theoretical foundation for developing AOFP-based functional foods with hypoglycemic properties, and offer insights for the precise application of traditional Chinese medicine polysaccharides in managing metabolic disorders.

Materials and Methods

Materials and chemicals

Alpinia oxyphylla fruits were purchased from Weiyuan Weiminyuan Biotechnology Co., Ltd. (Batch No.: 20241001). DEAE-52 cellulose and Sephadex G-100 were obtained from Shanghai YuanYe Biotechnology Co., Ltd. Pectinase, cellulase, and papain from Beijing Hongrun Baoshun Technology Co., Ltd. The strains of *A. niger* ATCC 16404 were provided by the laboratory of the School of Food Science and Engineering, Yangjiang Campus, Guangdong Ocean University. The 10 monosaccharide standards, including galacturonic acid, xylose, mannose, arabinose, rhamnose, ribose, glucose, galactose, glucuronic acid, and fructose, were provided by Yuanye Biotechnology Co., Ltd. (Shanghai, China). All chemical reagents used, including n-hexane, concentrated sulfuric acid, and phenol, were of analytical grade and were provided by Macklin Biochemical Co., Ltd.

Experimental methods

High-pressure high-temperature extraction (HH)

Polysaccharides were extracted from dried *A. oxyphylla* (50 °C, 48 h) using the HH method (Zheng *et al*., 2024). Briefly, 5 g powder (60-mesh) was extracted with water (1:20, w/v) at 121 °C/0.1 MPa for 30 min. After centrifugation (4000 rpm, 15 min), the supernatant was concentrated and precipitated with 80% ethanol (4 °C, 12 h). The crude polysaccharide was deproteinized using the Sevag method (chloroform/n-butanol = 4:1) (Shang *et al*., 2018; Wang *et al*., 2017), dialyzed (1kDa, 48h), purified by DE-52 cellulose column, and lyophilized to obtain AOFP-HH.

Acid-assisted high-pressure high-temperature extraction (AHP)

Dried *A. oxyphylla* fruits were oven-dried at 50 °C for 48 h until a constant weight was achieved, and ground to a particle size of less than 150 μm (60-mesh sieve). A 5.0 g portion of the powder was mixed with distilled water at a ratio of 1:20 (w/v), and the pH was adjusted to 3 using 1% hydrochloric acid. The mixture was homogenized and subjected to high-pressure steam treatment using the LDZF-50L sterilizer. The subsequent steps were identical to those described under "Materials and Methods", and the final product was designated as AOFP-AHP.

Aspergillus niger fermentation extraction (ANF)

Dried *A. oxyphylla* fruits were oven-dried at 50 °C for 48 h to reach constant weight and ground to a particle size of less than 150 μm (60-mesh sieve). A total of 5.0 g of powder was mixed with distilled water at a ratio of 1:20 (w/v) and sterilized in an autoclave. After cooling to room temperature, the mixture was inoculated with *A. niger* ATCC16404 (1×10^7–2×10^7 CFU/mL) at an inoculation volume of 5% (v/v). The fermentation was carried out at 30 °C at pH 5–6 for 16 h. The same steps described under "Materials and Methods" were followed, and the final product was named AOFP-ANF.

Structural characterization of *alpinia oxyphylla* polysaccharides

Molecular weight and monosaccharide composition analysis

Molecular weight was determined using a multiangle laser light scattering detector (DAWN HELEOS II) coupled with a differential refractive index detector (RID-20A) and Shodex OHpak SB-806M HQ/SB-804M HQ columns (300 mm × 7.8 mm, Japan) (Yin *et al*., 2021). The analysis was performed at 40 °C with 0.1 mol/L sodium nitrate (pH 5.5) as mobile phase at a 0.5 mL/ min flow rate. For monosaccharide composition analysis (Zeng *et al*., 2018), samples were hydrolyzed with trifluoroacetic acid (TFA) (121 °C, 2 h), evaporated under nitrogen, and washed with methanol (3×). The hydrolysates were filtered (0.22 μm) and analyzed using a Dionex ICS5000+ system equipped with a Carbopac PA-20 column (4 mm × 250 mm, USA). The mobile phase consisted of 97.5% ultrapure water (containing 0.25 mmol/L NaOH) and 2.5% 100 mmol/L NaOH solution (1.0 mL/ min, 30 °C). Monosaccharides (D-mannose, D-glucose, D-galacturonic acid, etc.) were quantified using standard references.

UV-Vis and fourier transform infrared spectroscopy (FT-IR)

Polysaccharide samples were prepared as 1 mg/mL aqueous solutions and scanned from 200 to 400 nm using quartz cuvettes (Li *et al*., 2025). For FT-IR analysis, freeze-dried polysaccharides were mixed with spectroscopic-grade KBr (1:100 w/w), ground into a homogeneous powder, and pressed into transparent pellets (verified by transmittance test (Shi *et al*., 2018)). Spectra were acquired on an FT-IR spectrometer (4000–400 cm^{-1}) at 4 cm^{-1} resolution with 64 cumulative scans (Zhao *et al*., 2023).

Congo red assay

Following optimized protocol (Song *et al*., 2025), 2 mg/ mL polysaccharide solutions were mixed with 160 μg/mL Congo red and gradient NaOH solutions (0–0.5 M, 0.1 M intervals) at a 2:1:1 volume ratio.

After vortexing and 10 min incubation, spectral scans (400–600 nm) were performed to record characteristic peak shifts of polysaccharide–Congo red complexes, using water as a blank control.

X-ray diffraction analysis

X-ray diffraction (XRD) analysis of AOFP samples was performed using a Shimadzu XRD-7000 diffractometer (Qian *et al*., 2009). Measurements were conducted over a 2θ range of 5–80°, with a counting time of 2 min per step and a step size of 0.02°. Lyophilized polysaccharide powders were evenly spread on a flat surface glass sample holder to avoid voids or agglomeration.

Scanning electron microscopy

Lyophilized polysaccharide samples were mounted on a metal stub and coated with a thin layer of gold. The surface morphology was observed using a high-resolution field-emission scanning electron microscope (SEM) (Apreo2S, Thermo Fisher Scientific, USA) at appropriate accelerating voltages and magnification levels (El-Gendi *et al*., 2023).

In vitro hypoglycemic assessment of AOFP

Determination of **α***-amylase inhibitory activity*

The α-amylase inhibitory activity assay was conducted following the method described by Yusoff *et al*. (2024) with minor modifications. A 5% starch solution, a 20 U/ mL α-amylase solution, polysaccharide samples at concentrations of 2, 4, 6, 8, and 10 mg/mL, and a positive control (acarbose) were prepared.

For the sample group (A_1), 300 μL of polysaccharide solution and 400 μL of α-amylase solution were added to a test tube. In the blank group (A_0), the same volume of distilled water and enzyme solution was added, while in the control group (A_2), the same concentrations of polysaccharide solution and buffer solution were used. All tubes were incubated at 37 °C in a biochemical incubator for 10 min. Then, 300 μL of soluble starch solution was added to each tube, followed by incubation at 37 °C for 15 min. Next, 2 mL of 3,5-Dinitrosalicylic Acid (DNS) reagent was added to develop color, and the tubes were heated on an electric stove for 10 min to inactivate the enzyme at high temperature. After cooling, the reaction mixture was brought to 10 mL with PBS, and the absorbance was measured at 540 nm. The inhibition rate of α-amylase activity was calculated using the following formula:

$$\alpha\text{-Amylase Inhibition Rate (\%)} = [1 - (A_1 - A_2) / A_0] \times 100\%$$

Determination of α-glucosidase inhibitory activity

The α-Glucosidase Inhibitory Activity assay was conducted following the method described by Tang *et al*. (2024), with minor modifications. A 2.5 mmol/L *p*-Nitrophenyl β-D-galactopyranoside (PNPG) solution, a 0.25 U/mL α-glucosidase solution, polysaccharide samples at concentrations of 2, 4, 6, 8, and 10 mg/mL, and a positive control (acarbose) were prepared. The assay was conducted using a 96-well microplate format.

For the sample group (A_1), 50 μL of polysaccharide solution and 50 μL of α-glucosidase solution were added to the wells. In the blank group (A_0), the same volumes of buffer and enzyme solutions were used, and in the control group (A_2), the same concentrations of polysaccharide solution and buffer were added. The plate was incubated at 37 °C in a biochemical incubator for 10 min. Then, 50 μL of PNPG solution was added to each well, and the mixture was shaken and incubated at 37 °C for 30 min. Absorbance was measured at 405 nm. Each sample was tested in triplicate (Tang *et al*., 2024). The inhibition rate of α-glucosidase activity was calculated using the following formula:

$$\alpha\text{-Glucosidase Inhibition Rate (\%)} = [1 - (A_1 - A_2) / A_0] \times 100\%$$

In vitro simulated digestion

Following the INFOGEST standardized protocol (Zhang *et al*., 2023), solutions of AOFP-HH, AOFP-AHP, and AOFP-ANF (4.0 mg/mL, 30 mL) were mixed with simulated saliva (30 mL) and incubated at 37 °C with 120 rpm shaking for 10 min at 120 rpm, followed by enzyme inactivation in a water bath at 95–100 °C for 5 min. After adding simulated gastric fluid (1:1, v/v) and repeating the incubation for 30 min, enzymes were inactivated again. Simulated intestinal fluid (10:3, v/v) was then added, with samples collected at 0 h and 4 h time points and immediately heat-inactivated (95–100 at 120 rpm, 5 min). The digestion products were lyophilized for subsequent molecular weight distribution and reducing sugar content analyses.

In vitro fermentation

Fecal sample collection and processing

Fresh fecal samples were collected from six healthy volunteers (3 males and 3 females, aged 18–25 years) who had not taken antibiotics within 3 months and had provided informed consent. Equal amounts of feces were pooled and homogenized in sterile PBS (pH 7.4) to prepare 10% (w/v) fecal slurry. The mixture was filtered through sterile gauze to obtain fecal inoculum, with all procedures completed within 2 h to maintain microbial community stability. The dietary information of the volunteers is shown in Table 1.

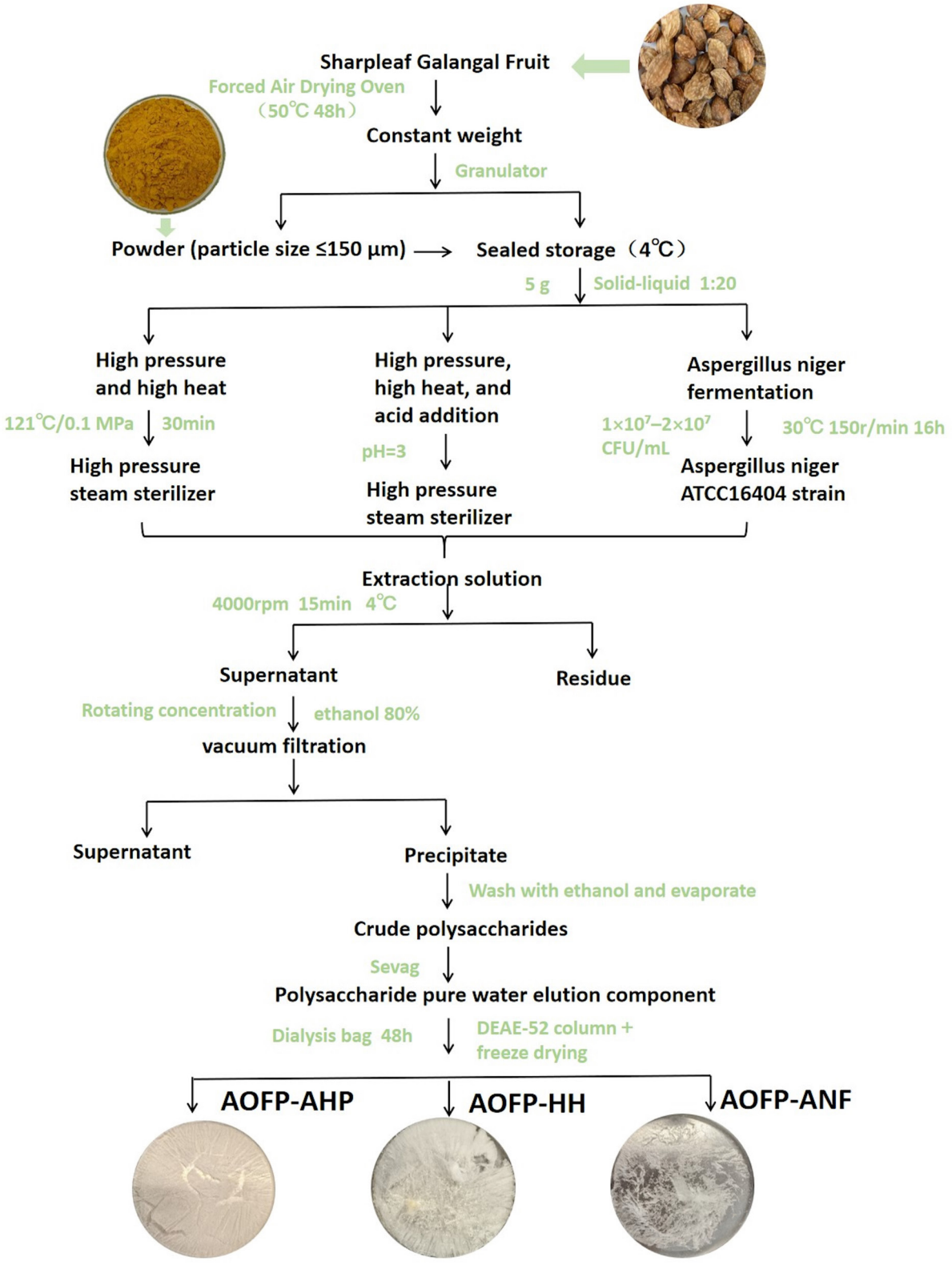

Figure 1. The extraction flowchart of AOFPs.

Table 1. Demographic characteristics, lifestyle, and dietary structure of the volunteers.

Characteristic	Gender	Age	Dietary characteristics	BMI	Smoke	Alcohol
1	Female	22	High fiber intake (35 g/day, whole grains + legumes), mixed diet (rice + fish/vegetables), low fat (25% energy), yogurt (5×/week)	19.5	No	No
2	Female	24	Moderate fiber (25 g/day, refined grains dominant), red meat (3×/week), high fat (35% energy), occasional alcohol (beer 1×/month)	22.4	No	1×/month
3	Female	20	Low fiber (15 g/day, fast food 4×/week), sugary drinks daily, normal fat (30% energy), no yogurt	23.5	No	No
4	Male	25	Balanced diet (whole grains + chicken/fish), fiber 30 g/day, Mediterranean style (olive oil, nuts), kombucha (3×/week)	21.9	No	No
5	Male	22	High-protein diet (whey supplements), fried food 2×/week, moderate fat (32% energy), beer (2×/month)	22.4	No	2×/month
6	Male	23	Vegetarian (tofu + tempeh), fiber 40 g/day, low fat (20% energy), kimchi daily	20.4	No	1×/month

Fermentation medium preparation

The culture medium was prepared according to the method of Zhang *et al*. (2023), with the following composition: resazurin (1 mg/L), peptone water (2 g/L), yeast extract (2 g/L), bile salts (0.5 g/L), hemin (5 mg/L), L-cysteine (0.5 g/L), vitamin K_1 (74.1 μL/L), NaCl (0.1 g/L), KH_2PO_4 (40 mg/L), K_2HPO_4 (40 mg/L), $MgSO_4{\cdot}7H_2O$ (0.01 g/L), $NaHCO_3$(2g/L), $CaCl_2{\cdot}6H_2O$ (0.01 g/L), Tween-80 (14.8 mg/L), and $Na_2S{\cdot}9H_2O$ (0.8 mmol/L). The prepared medium was sterilized by autoclaving and stored for later use.

In vitro fermentation procedure

The experiment included five groups (n = 3 replicates each): **AOFP-HH**, **AOFP-AHP**, and **AOFP-ANF** treatment groups; positive control (inulin, **JF group**); and blank control (fecal inoculum, **FJ group**). Exactly 200 mg of each sample was added to 9 mL medium in anaerobic tubes (Zhang *et al*., 2025). After sterilization (121 °C, 20 min) and cooling, 1 mL fecal inoculum was inoculated. Fermentation proceeded anaerobically (37 °C) for 48 h, with samples collected at 12, 24, 36, and 48 h for pH measurement, reducing sugar content, and monosaccharide composition analysis.

Determination of short-chain fatty acids

The concentrations of short-chain fatty acids (SCFAs), including acetic acid, propionic acid, and butyric acid, were determined using gas chromatography, with slight modifications based on previously reported methods (Wang *et al*., 2012). Briefly, 400 μL of 0.2 mol/L hydrochloric acid solution containing 0.3 mg/mL of 2-ethylbutyric acid (as internal standard) was mixed with 400 μL of the sample or standard solution. After centrifugation at 8000 rpm for 5 min, 1 μL of the supernatant was injected into the gas chromatograph. An HP-INNOWAX capillary column (30 m × 0.25 mm × 0.25 μm, Agilent) was used. Nitrogen (N_2) served as the carrier gas at a flow rate of 19.0 mL/min. The flow rates for air, hydrogen, and nitrogen makeup gas were 260, 30, and 30 mL/min, respectively. The temperature program was set as follows: initial temperature of 60 °C held for 2 min, increased to 180 °C at 20 °C/min and held for 2 min, then increased to 220 °C at 4°C/min and held for 2 min.

Microbial community amplicon sequencing

Sequencing was performed by Guangzhou Gidio Biotech Co., Ltd. Following DNA extraction using the HiPure Stool DNA Kit, the V3-V4 regions of 16S rRNA genes were amplified via PCR (95 °C for 5 min; 30 cycles of 95 °C/1 min, 60 °C/1 min, 72 °C/1 min; final extension at 72 °C for 7 min) in a 50 μL reaction system containing 10 μL 5 × Q5 Reaction Buffer, 10 μL 5 × Q5 High GC Enhancer, 1.5 μL 2.5 mM dNTPs, 1.5 μL each of 10 μM primers, 0.2 μL Q5 High-Fidelity DNA Polymerase, and 50 ng template DNA. Amplified products were quality checked by 2% agarose gel electrophoresis, purified using AMPure XP Beads, quantified using Qubit 3.0, and processed into libraries with the Illumina DNA Prep Kit before being sequenced on the NovaSeq 6000 platform (PE250 mode) after passing quality control on an ABI Step One Plus system.

Statistical analysis

All experimental data were collected from three independent replicates and expressed as mean ± standard deviation (SD). Statistical analyses were performed using SPSS (version 26.0, IBM Corp.), with one-way ANOVA followed by Tukey's post-hoc test for multiple comparisons ($P < 0.05$ considered statistically significant). Graphical representations were generated using OriginPro 2022 (OriginLab Corporation), with error bars denoting SD. For microbiome data, alpha-diversity indices (Shannon, Chao1) and beta-diversity

metrics (Bray–Curtis dissimilarity) were calculated in QIIME2, and PERMANOVA was used to assess group differences.

Results and Discussion

Characterization of AOFP

Molecular weight and monosaccharide composition

Extraction methods significantly influenced polysaccharide yield and structural characteristics (Yin *et al.*, 2024). AOFP-AHP showed the highest yield (28.38% ± 0.21), attributed to H^+-catalyzed hydrolysis of cell wall cellulose/hemicellulose glycosidic bonds by HCl (Liu *et al.*, 2024), which enhanced intracellular polysaccharide release (Chi *et al.*, 2018). AOFP-ANF exhibited intermediate yield (22.62% ± 0.39), while AOFP-HH had the lowest (13.65% ± 0.41) due to the absence of chemical degradation. Molecular weight distribution revealed method-dependent variations: AOFP-HH (4.07 kDa) maintained the highest MW through high-pressure hydrogen bond association, while AOFP-AHP (1.03 kDa) showed acid-induced β-(1→3) glycosidic bond cleavage, and AOFP-ANF (1.14 kDa) exhibited enzymatic hydrolysis effects. Monosaccharide composition analysis demonstrated structural heterogeneity; AOFP-HH contained glucose (67.33%) and galacturonic acid (11.74%), AOFP-AHP was exclusively glucose (100%), and AOFP-ANF was predominantly glucose (97.01%) with minor concentrations of glucuronic acid (0.38%) and arabinose (1.26%), collectively highlighting how processing methods dictate structural features that underlie bioactivity differences.

UV-Vis and FT-IR spectral characterization

UV-Vis analysis (Figure 2A) revealed that AOFP-ANF exhibited significantly higher absorbance in the 200–400 nm range compared to AOFP-HH and AOFP-AHP, suggesting the presence of more conjugated structures or chromophores. All samples showed weak absorption peaks at 260 nm (nucleic acids) and 280 nm (proteins), with absorbance values (<0.2) confirming impurity levels below the detection limit, meeting polysaccharide purity requirements. FT-IR spectral analysis (Figure 2B) demonstrated highly similar functional group characteristics among the three polysaccharides: a broad peak at 3400 cm^{-1} (O-H stretching vibration, hydrogen

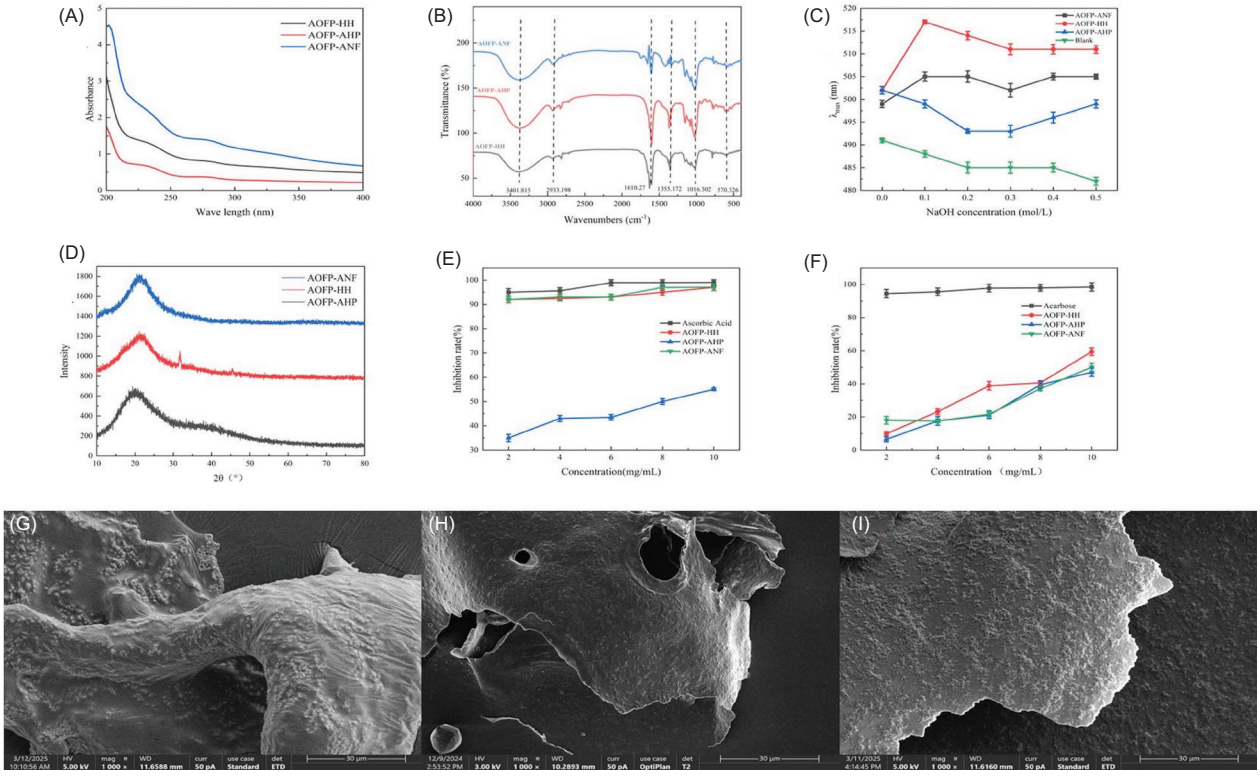

Figure 2. The structural and functional characterization of three AOFPs: (A) UV-Vis absorption spectra; (B) Fourier transform infrared (FTIR) spectra; (C) Congo red assay results; (D) X-ray diffraction (XRD) patterns; (E) α-Amylase inhibition rates; (F) α-Glucosidase inhibition rates; (G-I) Scanning electron micrographs (SEM) at 1000× magnification: (G) AOFP-HH, (H) AOFP-AHP, (I) AOFP-ANF.

bonding), 2933 cm^{-1}(C-H asymmetric stretching of CH_2/CH_3 groups) (Wang *et al*., 2012), 1610 cm^{-1} (weak C=O asymmetric vibration, possibly from residual esters or proteins, consistent with UV results), 1355–1020 cm^{-1} (fingerprint region with C-O-H bending and pyranose ring C-O-C vibrations, indicating β-(1→4) glycosidic linkages) (Kačuráková *et al*., 2000), and 570 cm^{-1} (characteristic of β-pyranose C1-OH axial conformation). Method-specific differences were observed, with AOFP-AHP showing a weak absorption peak at 1740 cm^{-1}, suggesting acid-induced ester bond formation. Chemical composition analysis (Table 2) revealed that AOFP-HH contained 11.74% galacturonic acid (GalA), while AOFP-AHP showed no detectable uronic acids. The intensity difference at 1740 cm^{-1} (characteristic C=O ester vibration) between these two samples indicates that acidic conditions may suppress uronic acid vibrations through steric hindrance. In conclusion, FT-IR spectroscopy confirmed that all three AOFP primarily contain β-(1→4) glycosidic linkages, with different extraction methods leading to esterification features in AOFP-AHP and extraction condition-dependent suppression of uronic acid vibrational signals.

Congo red assay analysis

The triple-helix conformation of polysaccharides, a critical structural feature closely associated with their functional activities, can be characterized through Congo red binding assays. When interacting with triple-helical polysaccharides, Congo red forms complexes that exhibit a characteristic red shift in maximum absorption wavelength (λmax) (Zeng *et al*., 2022), which diminishes upon triple-helix disruption by strong alkali. Our results revealed significant differences in λmax responses to NaOH concentration among the polysaccharides (Figure 2C): both AOFP-HH and AOFP-ANF maintained pronounced red shifts across tested concentrations, indicating preserved triple-helix stability, whereas AOFP-AHP showed minimal red shift, suggesting conformational disruption likely caused by acid-induced hydrogen bond cleavage during extraction.

Table 2. Monosaccharide composition and molecular weight (mol%) of three polysaccharides obtained by different extraction methods.

Samples	AOFP–HH	AOFP–AHP	AOFP–ANF
Man	3.1965	–	0.9822
Rha	–	–	0.3609
GlcA	–	–	0.3823
GalA	11.7405	–	–
Glc	67.3359	100	97.0111
Gal	5.7209	–	–
Xyl	5.3015	–	–
Ara	6.7048	–	1.2634
Molecular weight	4.07 kDa	1.03 kDa	1.14 kDa

The stability of intra- and intermolecular hydrogen bonds fundamentally determines the triple-helix integrity. Hydrogen bond disruption triggers conformational transitions under strong alkali or high temperature conditions, the triple helix unwinds into random coils, leading to decreased λmax of Congo red complexes (Pan *et al*., 2025). In our study, AOFP-HH and AOFP-ANF demonstrated more robust hydrogen-bonding networks that maintained conformational stability, whereas the presumably weaker hydrogen bonding in AOFP-AHP, potentially due to altered side-chain structures or substitution patterns, resulted in greater environmental sensitivity.

These findings further support the positive correlation between triple-helix integrity and bioactivity. For instance, lentinan exhibits hepatoprotective and testicular protective effects attributed to its stable triple-helix structure (Cao *et al*., 2019). Given their conformational stability, AOFP-HH and AOFP-ANF may possess similar bioactive potential, whereas the functionality of AOFP-AHP might be compromised by structural instability.

XRD analysis

Crystal structure analysis of the three AOFPs was performed using a Shimadzu XRD-7000 diffractometer (Figure 4D). The XRD patterns revealed that both AOFP-ANF and AOFP-AHP displayed no significant diffraction peaks within the 10–80° scanning range, characteristic of amorphous polymers. This observation aligns with the typical properties of plant-derived polysaccharides, as conventional water extraction methods often yield amorphous structures due to disordered molecular chain arrangements and aperiodic hydrogen bonding networks (Jiang *et al*., 2020).

Notably, AOFP-HH exhibited a distinct diffraction peak at 32°, corresponding to the interplanar spacing of β-(1→3)-glucan chains, suggesting the presence of highly ordered glucan segments (Li *et al*., 2016). The crystalline nature of AOFP-HH is closely associated with its extraction parameters (high temperature and pressure): elevated temperature (121 °C) likely promotes the reorganization of intramolecular hydrogen bonds, while high pressure (0.1 MPa) mechanically aligns the polymer chains. This synergistic effect facilitates the formation of localized crystalline regions in AOFP-HH, rich in β-1,3-glucan chains with glucose residues, thereby generating the characteristic XRD peak (Sun *et al*., 2025).

Although the AHP method also involves high temperature and pressure, the acidic conditions (pH 3.0) cleave glycosidic bonds, leading to molecular depolymerization. Similarly, while the ANF method produces low-molecular-weight fragments via microbial degradation, enzymatic hydrolysis tends to cause random scission rather than ordered rearrangement, preventing crystalline structure formation in both cases (Zhang *et al*., 2023). In conclusion, the HH method yields polysaccharides with highly ordered glucan segments and crystalline structures, offering new insights into the three-dimensional regulation of process-structure-function relationships for industrial polysaccharide production.

SEM analysis

As shown in Figures 2G–2I, the three AOFPs exhibited distinct micromorphologies at 1000× magnification under SEM, directly reflecting the regulatory effects of extraction methods on polysaccharide surface structures: AOFP-HH (Figure 2G) displayed folded structures after high-pressure and high-temperature treatment. The thermal process likely activated interchain hydrogen bonding networks, promoting ordered alignment and lamellar stacking (Shi *et al*., 2020), manifesting as periodic wrinkles macroscopically. AOFP-AHP showed curled lamellar morphology (Figure 2F) under acidic conditions. Acid-catalyzed hydrolysis selectively cleaved α-1,6-glycosidic bonds while preserving the rigid β-pyranose rings, resulting in curled main-chain fragments forming scale-like aggregates (Yang *et al*., 2022), consistent with its amorphous XRD pattern. AOFP-ANF (Figure 2I) presented flattened two-dimensional sheets with surface protrusions after enzymatic treatment. The preferential degradation of β-1,4-glycosidic bonds generated low-molecular-weight fragments that formed disordered lamellar stacks due to steric hindrance (Liberato *et al*., 2021).

The SEM data correlated well with XRD crystallinity and analysis-folded structures corresponded to semi-crystalline states, while disordered surfaces matched amorphous characteristics. These findings demonstrate that extraction processes directly influence polysaccharide morphology and physical properties through molecular-level regulation (hydrogen bond reorganization/glycosidic bond cleavage/random degradation), providing structural design guidelines for functional applications.

In vitro hypoglycemic activity of polysaccharides

α-amylase inhibitory activity

The α-amylase inhibitory effects of polysaccharides (AOFP-HH, AOFP-AHP, and AOFP-ANF) obtained through different extraction methods were evaluated using in vitro enzyme inhibition assays. As shown in Figure 2E, all three polysaccharides exhibited significant concentration-dependent inhibition. At the highest tested concentration (10.0 mg/mL), AOFP-HH and AOFP-AHP demonstrated comparable inhibition rates (97 and 97.08%, respectively), which were significantly higher than that of AOFP-ANF (95.5%). This observation suggests that the extraction method may have a weaker influence on inhibitory activity than the inherent structural characteristics of the polysaccharides. Further analysis revealed that the strong inhibitory activity of AOFP-HH and AOFP-AHP may be attributed to their rigid structures formed by β-(1→3) glycosidic bonds, which can effectively block enzyme–substrate binding through steric hindrance effects (Zheng *et al*., 2024). On the other hand, AOFP-ANF likely underwent partial glycosidic bond cleavage during extraction, resulting in increased molecular flexibility. This more flexible chain conformation may render AOFP-ANF more susceptible to enzymatic degradation, thereby reducing its inhibition efficiency.

α-glucosidase inhibitory activity

α-Glucosidase inhibitors act by competitively binding to active sites (such as the −1 and +1 subsites within the catalytic pocket) of α-glucosidase on the brush border membrane of the small intestine, which leads to a delay in carbohydrate hydrolysis into monosaccharides and reduction of postprandial blood glucose spikes (Song *et al*., 2020). The α-glucosidase inhibition assay (Figure 2F) revealed distinct inhibitory patterns among the three polysaccharides. Though there were minor fluctuations at concentrations of 2–5 mg/mL, all samples exhibited marked concentration-dependent increases in inhibition within the 5–10 mg/mL range. Notably, at 10.0 mg/ mL, AOFP-HH demonstrated superior inhibitory activity (59.43%), significantly outperforming AOFP-AHP (50.04%) and AOFP-ANF (47%). This differential activity may be attributed to several structural characteristics: The predominance of β-(1→3) glycosidic bonds in AOFP-HH creates a rigid structure that effectively blocks enzyme–substrate binding through steric hindrance; Its higher molecular weight potentially exposes more active sites; The high-pressure and high-temperature (HH) extraction better preserves triple-helix conformations while disrupting cell walls, whereas acidic AHP conditions cleave glycoside bonds and reduce active fragment exposure. Furthermore, the elevated galacturonic acid content (11.74%) in AOFP-HH enhances hydrogen-bonding capacity with enzyme active sites through catechol groups. This aligns with the known mechanism of α-glucosidase inhibitors, which primarily interact with substrates via hydrogen bonds and van der Waals forces (Xiang *et al*., 2024).

The AOFP-HH extracted by the HH method exhibited the highest inhibitory activity against α-amylase

and α-glucosidase. Studies have shown that the rigid structure of β-1,3-glucan can sterically hinder enzyme–substrate binding, while carboxyl groups enhance intermolecular interactions through hydrogen-bonding networks, further stabilizing the conformation (Li *et al*., 2020). This finding is consistent with the research by Chen *et al*. (2019) on shiitake polysaccharides, where the triple-helix structure of β-1,3-glucan was found to be key to its antitumor activity. Additionally, the Congo red assay demonstrated that AOFP-HH maintains a triple-helix conformation even under strongly alkaline conditions, indicating superior structural stability, which may be a crucial factor in its high activity. Although AOFP-AHP showed a lower α-glucosidase inhibitory rate of 50.04%, the disappearance of the ester bond absorption peak suggests that acidic conditions disrupt the carboxyl groups of uronic acids, leading to dissociation of the hydrogen-bonding network (Kačuráková *et al*., 2000). This is consistent with the study by Sun *et al*. (2025) on kelp polysaccharides, where acid treatment randomly cleaves glycosidic bonds, reducing molecular order and weakening biological activity. Notably, the α-amylase inhibitory rate of AOFP-AHP (97.08%) was comparable to that of the HH group, possibly due to the retention of some β-1,3-glucan fragments; however, the significant difference in α-glucosidase inhibitory activity underscores the importance of structural integrity for specific enzyme targets. The low α-glucosidase inhibitory rate of AOFP-ANF may be related to the preferential utilization of low-molecular-weight fragments (such as mannose) produced during fermentation by microorganisms (Chen *et al*., 2019). Research indicates that short-chain oligosaccharides are more readily metabolized by gut microbiota but may lack effective binding capacity to the active sites of α-glucosidase (Xiang *et al*., 2024). Furthermore, the absence of characteristic diffraction peaks in the XRD pattern of AOFP-ANF indicates an amorphous structure that is incapable of forming a stable triple helix, limiting its activity.

In vitro digestibility of AOFP

The simulated digestion experiments revealed significant differences in the degradation behavior of AOFPs across digestive phases (Figures 3A–3C). During oral digestion (10 min), the minimal release of reducing sugar (0.8 mg/ mL) indicated limited degradation by salivary amylase. Gastric digestion showed progressive increases in reducing sugars (2.7 mg/mL at 30 min; 3.1 mg/mL at

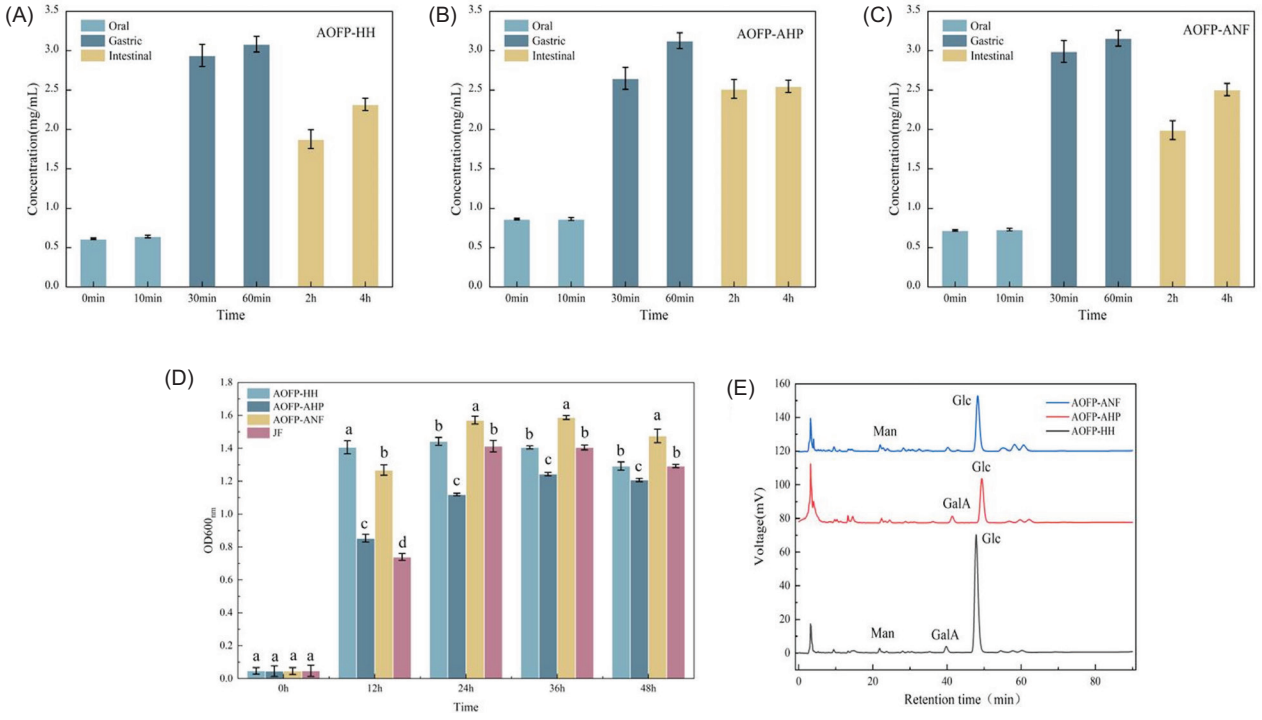

Figure 3. Physicochemical and microbial changes of AOFPs during simulated digestion and in vitro fermentation: (A) Reducing sugar content during AOFP-HH digestion; (B) Reducing sugar content during AOFP-AHP digestion; (C) Reducing sugar content during AOFP-ANF digestion; (D) Bacterial growth dynamics during in vitro fecal fermentation; (E) Monosaccharide profile changes during in vitro fecal fermentation.

60 min), attributed to the nonspecific glycosidic bond cleavage by gastric acid and pepsin. Interestingly, the intestinal phase exhibited a slight reduction in reducing sugars, likely due to further breakdown into absorbable oligosaccharides/monosaccharides through intestinal mucosal uptake (Wang *et al*., 2024).

Structural transformations of AOFPs during in vitro fermentation and effect on gut microbiota

Growth kinetics analysis of gut microbiota

Monitoring of OD_{600} values during in vitro fecal fermentation (Figure 3D) demonstrated that all three AOFPs significantly enhanced gut microbiota growth but exhibited distinct kinetic patterns: AOFP-HH showed rapid early-phase proliferation (OD 1.38 at 12h), peaking at 24 h (OD 1.42) before gradual decline; AOFP-ANF displayed the strongest growth-promoting effects, reaching maximum OD (1.58) at 24 h and maintaining sustained high levels, while AOFP-AHP exhibited slower growth kinetics, requiring 48 h to approach comparable levels (Yang *et al*., 2021). The superior microbiota-stimulating capacity of AOFP-ANF (extracted via *A. niger* fermentation) likely stems from its higher content of readily metabolizable low-molecular-weight components that preferentially support bacterial proliferation.

Dynamic pH changes in fermentation systems

The pH evolution profiles during fermentation (Figure 4A) further elucidated the metabolic characteristics of different AOFPs. All AOFP-treated groups exhibited significantly lower pH values compared to the blank control (FJ group, pH 6.1), indicating substantial production of acidic metabolites through microbial polysaccharide fermentation. Specifically, the AOFP-ANF group showed a continuous pH decline (12 h: 4.0 → 48 h: 3.2), consistent with its OD value changes, whereas AOFP-HH and AOFP-AHP displayed fluctuating decreases with transient midphase recoveries. These differences likely reflect structural heterogeneity among AOFPs, containing both readily fermentable oligosaccharide components and high-molecular-weight fractions requiring prolonged degradation.

Changes in monosaccharide composition

Postfermentation monosaccharide analysis (Figure 3E) revealed distinct metabolic patterns. In the AOFP-HH group, glucose (Glc) content significantly increased (67.33%→93.87%), and galacturonic acid (GalA) decreased (11.74%→4.06%). The newly emerged mannose (Man, 2.07%) indicated preferential degradation of GalA side chains via β-galacturonidase and concomitant release of Man units from RG-I regions. The AOFP-AHP group transitioned from a homogeneous Glc polymer to a mixture containing GalA (11.21%) and Man (3.58%), with a 14.79% reduction in Glc, suggesting endo-mannanase-mediated backbone cleavage and pectin lyase-triggered liberation of cryptic GalA branches. The AOFP-ANF group showed complete consumption of arabinose (Ara) and appearance of Man (3.83%), demonstrating prioritized Ara utilization and mannosidase-driven backbone depolymerization. Notably, all three AOFPs produced Man components postfermentation via multiple mechanisms, including cleavage of polysaccharide backbones by mannosidases from core microbiota (Chen *et al*., 2019), phosphorylase-catalyzed release of Man residues, and cross-feeding between bacterial species. These findings offer critical molecular-level evidence for understanding AOFP prebiotic functions.

Characteristics of short-chain fatty acid production

Butyrate production characteristics

In vitro fermentation results (Figure 4B) demonstrated significant butyrogenic advantages across all three AOFP treatment groups (HH, AHP, ANF). During early fermentation (12–24 h), each AOFP group exhibited substantially higher butyrate production (0.055–0.081 mmol/L) compared to the blank (FJ, 0.025–0.038 mmol/L) and positive control (JF, 0.017–0.028 mmol/L).

Notably, the AOFP-AHP group reached peak butyrate production at 24 h (0.081 mmol/L), while AOFP-HH sustained elevated levels (0.076 mmol/L) through 48 h, approximately double the output of the FJ group. This early-stage butyrate surge likely reflects selective stimulation of butyrate-producing bacteria (e.g., *Butyricicoccus, Faecalibacterium*) by β-(1→3) glycosidic bonds in AOFP structures.

Acetate metabolic dynamics

The acetate production kinetics revealed distinct metabolic patterns among groups (Figure 4C): AOFP-HH and AHP exhibited rapid early-phase accumulation (>0.37 mmol/L at 12 h) followed by gradual decline, whereas AOFP-ANF showed delayed production (0.01 mmol/L at 12 h) with a dramatic 60-fold increase by 24 h (0.62 mmol/L). In contrast, the JF positive control exhibited characteristic delayed-peak kinetics, reaching maximum yield (0.92–0.95 mmol/L) at 36 h. These differential patterns reflect carbon source-specific regulation of microbial metabolic pathways. Specifically, the accessible oligosaccharides of AOFP-HH/AHP drove immediate acetogenesis, the complex structure of AOFP-ANF required prolonged enzymatic processing, and the standard prebiotic components of JF induced late-phase fermentation. The temporal stratification (early/mid/late-phase peaks) demonstrates structure-dependent carbohydrate accessibility governing microbial acetate synthesis dynamics.

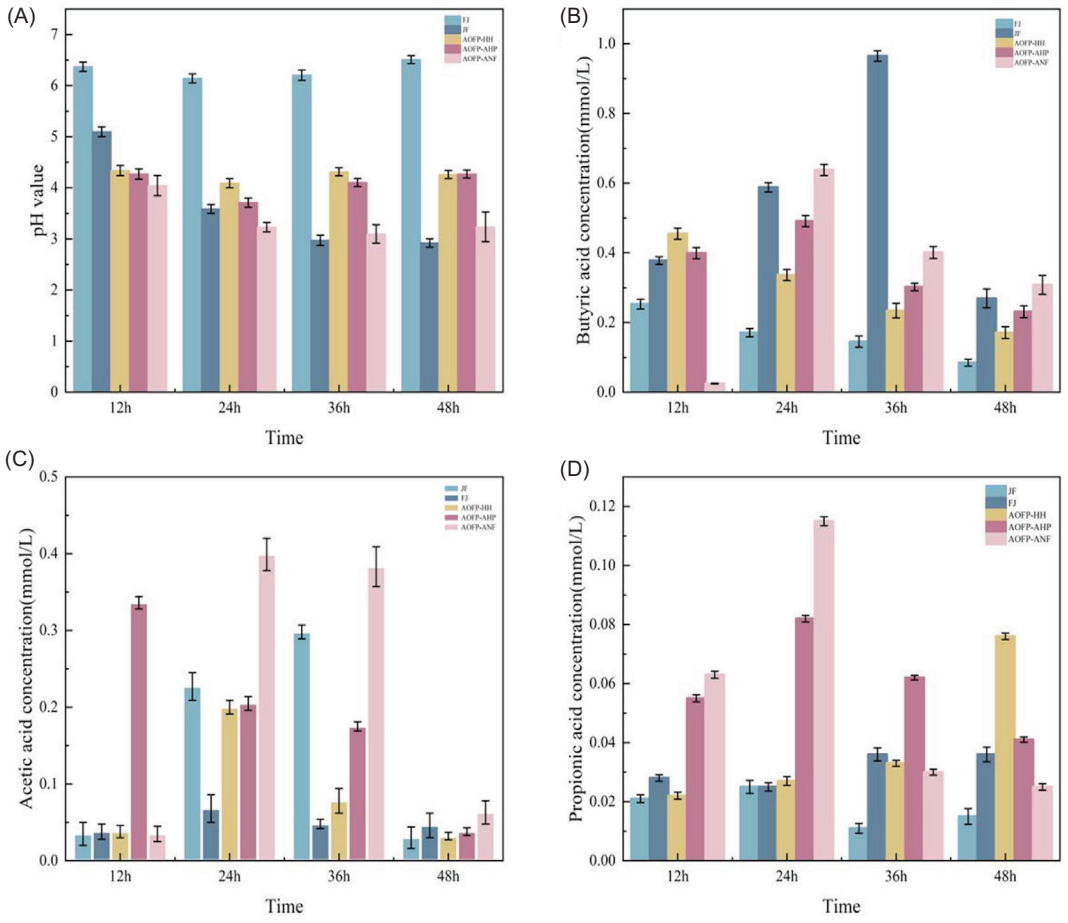

Figure 4. Changes in pH, acetic acid, propionic acid, and butyric acid during in vitro fecal fermentation: (A) Changes in pH during AOFP-HH, AOFP-AHP and AOFP-ANF fermentation; (B) Changes in butyric acid during AOFP-HH, AOFP-AHP and AOFP-ANF fermentation; (C) Changes in acetic acid during AOFP-HH, AOFP-AHP and AOFP-ANF fermentation; (D) Changes in propionic acid during AOFP-HH, AOFP-AHP and AOFP-ANF fermentation.

Propionate production patterns

The propionate generation dynamics exhibited significant intergroup variations (Figure 4D): AOFP-HH and AHP groups produced relatively high propionate levels (0.33 mmol/L) during the early phase (12 h), followed by a rapid decline. On the other hand, the positive control (JF) showed an increasing trend, reaching peak production (0.40 mmol/L) at 48 h, while the blank control (FJ) maintained consistently low levels (≤0.10 mmol/L). These kinetic patterns suggest that AOFPs may preferentially activate the glycolytic pathway for propionate generation, whereas JF likely promotes continuous propionate production via the succinate pathway. Our findings reveal three key insights. First, AOFPs drive early-phase butyrate production, while JF shows mid-to-late-phase acetate and propionate patterns. Second, the rigid structure of AOFPs may selectively enhance colonization and metabolism of butyrate-producing bacteria (Liu *et al.*, 2025). Third, AOFP-HH rapidly produces acetate for the energy needs of enterocytes, AOFP-AHP sustains propionate for lipid regulation, and all AOFPs prioritize butyrate to support gut barrier integrity. These results provide a mechanistic framework for understanding how polysaccharide structures differentially modulate gut microbial metabolic networks, while establishing a theoretical foundation for developing SCFA-targeted functional polysaccharide products.

All AOFP groups significantly promoted the proliferation of butyrate-producing bacteria. This is consistent with Wang *et al.*'s (2025) research on fructooligosaccharides, where polysaccharides improve gut barrier function by promoting the growth of butyrate-producing bacteria (such as Faecalibacterium).

Species composition analysis

Phylum-level microbial composition

Microbiome analysis (Figure 5A) revealed distinct phylum-level patterns among groups, with Bacillota, Pseudomonadota, Fusobacteriota, and Actinomycetota dominating: AOFP-AHP showed the highest Bacillota abundance (implicating both probiotic [e.g., *Bacillus subtilis* surfactin production] and pathogenic [e.g., *Bacillus cereus* toxin] potentials), while all AOFPs suppressed Pseudomonadota (containing pathogens like *Pseudomonas aeruginosa*) more effectively than JF controls. Notably, AOFP-ANF uniquely enriched Fusobacteriota, a phylum with dual roles in immune regulation (Treg/IL-10 activation) and disease (Fap2-mediated CRC progression), suggesting extraction-method-dependent modulation of microbial ecosystems with therapeutic implications.

Microbiome profiling (Figure 5A) showed distinct community structures. The dominant phyla were Bacillota, Pseudomonadota, Fusobacteriota, and Actinomycetota. Three key findings emerged. First, Bacillota abundance followed AOFP-AHP > AOFP-HH > AOFP-ANF > FJ > JF. This phylum showed functional duality. Probiotic *B. subtilis* enhanced gut barrier through surfactin-mediated pathogen inhibition, NLRP6 activation, and β-glucanase-derived SCFAs. Pathogenic *B. cereus* produced mitochondrial toxins. Second, all AOFPs significantly suppressed Pseudomonadota. The suppression order was as follows: AOFP-HH > AOFP-AHP > AOFP-ANF. This phylum contained opportunistic pathogens like *P. aeruginosa*, and disrupted tight junctions via rhamnolipids and triggered NLRP3/IL-1β inflammation (Lin *et al*., 2025). Third, AOFP-ANF uniquely enriched Fusobacteriota. The enrichment was in the order AOFP-ANF > FJ > JF > AOFP-HH > AOFP-AHP. This phylum had context-dependent roles. Beneficial strains excluded pathogens, stimulated Treg/IL-10, and synthesized butyrate. Pathogenic variants promoted CRC via Fap2 binding, β-catenin activation, and TLR4/MyD88-driven cytokine production. This suggests the selective immunomodulatory potential of AOFP-ANF through microbial manipulation.

Genus-level taxonomic composition

Analysis of genus-level community structure (Figure 5B) identified the top 10 dominant genera as *Megamonas,*

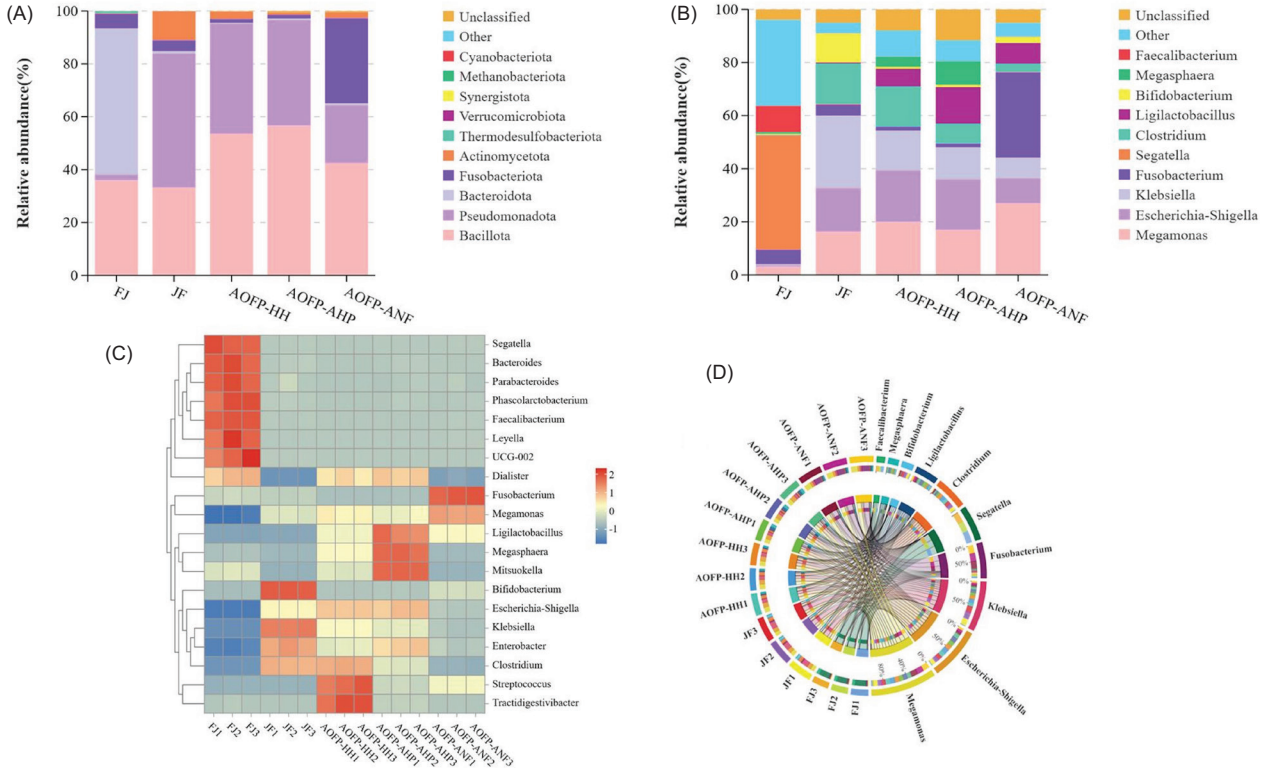

Figure 5. Species composition analysis and Flagship Species Analysis: (A) Composition of gut microbiota at the phylum level; (B) Composition of gut microbiota at the genus level; (C) Gut microbiota analysis based on genus-level heatmap; (D) Gut microbiota analysis based on genus-level Circos plot.

Escherichia-Shigella, Klebsiella, Fusobacterium, Segatella, Clostridium, Ligilactobacillus, Bacteroides, Bifidobacterium, *Megasphaera*, and *Faecalibacterium*. Comparative analysis revealed that AOFP-HH, AOFP-AHP, and AOFP-ANF groups exhibited significantly higher abundance of *Ligilactobacillus* than the FJ group ($P < 0.05$), with its proliferation negatively correlating with *Segatella* abundance. Notably, *Fusobacterium* was uniquely enriched in the AOFP-ANF group. *Ligilactobacillus* exerts probiotic effects through multiple mechanisms. It secretes bacteriocins that directly inhibit pathogens. The bacterium enhances the intestinal tight-junction protein expression, which helps repair the physical barrier. Additionally, it promotes regulatory T cell differentiation, which downregulates IgE-mediated allergic responses and improves gut immune homeostasis (Wang *et al*., 2025). *Segatella*, a gram-negative opportunistic pathogen, exerts multiple pathogenic effects. It secretes IgA protease to degrade mucosal sIgA, compromising immune barrier function. The pathogen activates the TLR4/MyD88 pathway, inducing proinflammatory IL-8 release and neutrophil recruitment, which worsens intestinal inflammation. Clinical studies associate its abundance with antibiotic-associated diarrhea severity and FMT failure in ulcerative colitis patients. Additionally, its metabolite, kynurenine, disrupts neurotransmitter balance, potentially exacerbating neurobehavioral abnormalities in ASD through the gut–brain axis. These findings suggest that AOFP intervention may optimize gut microbiota composition and modulate mucosal immunity by regulating the competitive interplay between *Ligilactobacillus* and *Segatella*.

Signature species divergence and community structure analysis

The Circos plot (Figure 5C) shows intergroup differences in microbial composition. Three key patterns emerged. First, probiotic dynamics were observed. AOFP groups had higher *Ligilactobacillus* abundance than FJ/JF controls, shown by thicker connecting lines. Its proliferation correlated with intestinal barrier integrity scores in a dose-dependent manner. This genus may function through two pathways. It modulates inflammation via LPS synthesis. It also produces butyrate, activating GPR41/43 receptors for immune regulation. Second, microbial succession occurred. Early *Bifidobacterium* proliferation was later replaced by *Lactobacillus*. AOFP-mediated pH reduction likely altered microbial competition. Bacteriocins secreted by *Lactobacillus* inhibited pathogen colonization, and their abundance negatively correlated with serum IL-6 and TNF-α levels. Third, network topology differed. Outer sectors represent sample groups, while inner sectors display core microbiota. Connecting line features indicate interaction strength. AOFP groups formed dense *Lactobacillus*-centric networks. On the other hand, FJ/JF groups showed *Bacteroides/Prevotella*-dominated structures. This divergence may influence host immunometabolic homeostasis.

Heatmap analysis of species composition (Figure 5D) revealed significant microbial community differentiation between AOFP-treated and FJ/JF control groups, with distinct group-specific patterns: AOFP-HH was characterized by *Tractidigestivibacte*r and *Streptococcus* as signature taxa; AOFP-AHP showed marked enrichment of *Mitsuokella, Megasphaera*, and *Ligilactobacillus*; while AOFP-ANF exhibited unique dominance of *Fusobacterium* and *Megamonas* (standardized abundance values are significantly higher than other groups, represented by dark red blocks in the heatmap). In contrast, FJ/JF controls were dominated by *Segatella, Bacteroides, Parabacteroides, Phascolarctobacterium, Faecalibacterium, Leyella*, and *UCG-002*. Hierarchical clustering confirmed separate evolutionary branches for AOFP and control groups, suggesting treatment-induced systematic modulation of microbiota structure through altered gut environments (e.g., pH, oxygen levels, or nutrient competition). Notably, the enrichment of acid-producing bacteria (e.g., *Streptococcus*) in AOFP groups contrasted with the *Bacillota* (e.g., *Leyella*) dominance in controls, a divergence likely influencing SCFA metabolic profiles and providing directional clues for functional investigations. Collectively, AOFP intervention remodeled gut microbiota by promoting probiotic colonization and suppressing opportunistic pathogens, likely through metabolite-driven immunomodulation and altered microbial competition.

Microbial community diversity analysis based on venn diagrams

The Venn diagram analysis (Figure 5A) of the five groups (FJ, JF, AOFP-HH, AOFP-AHP, AOFP-ANF) identified 2,169 OTUs, with only 50 core OTUs shared across all groups. Group-specific distributions showed FJ possessed the highest number of unique OTUs (676), followed by AOFP-AHP (513), AOFP-ANF (395), AOFP-HH (396), and JF (189). Among AOFP treatments, AOFP-HH exhibited the greatest microbial diversity (most unique species), while AOFP-AHP and AOFP-ANF showed reduced diversity, potentially due to polysaccharide extraction methods simplifying community structure. Notably, just three OTUs were common to all AOFP groups, indicating substantial functional or metabolic divergence, while greater OTU overlap between AOFP-HH and AOFP-ANF suggests shared regulatory mechanisms.

Alpha diversity analysis

Alpha diversity analysis (Figures 6A–6F) revealed significant differences in gut microbiota diversity

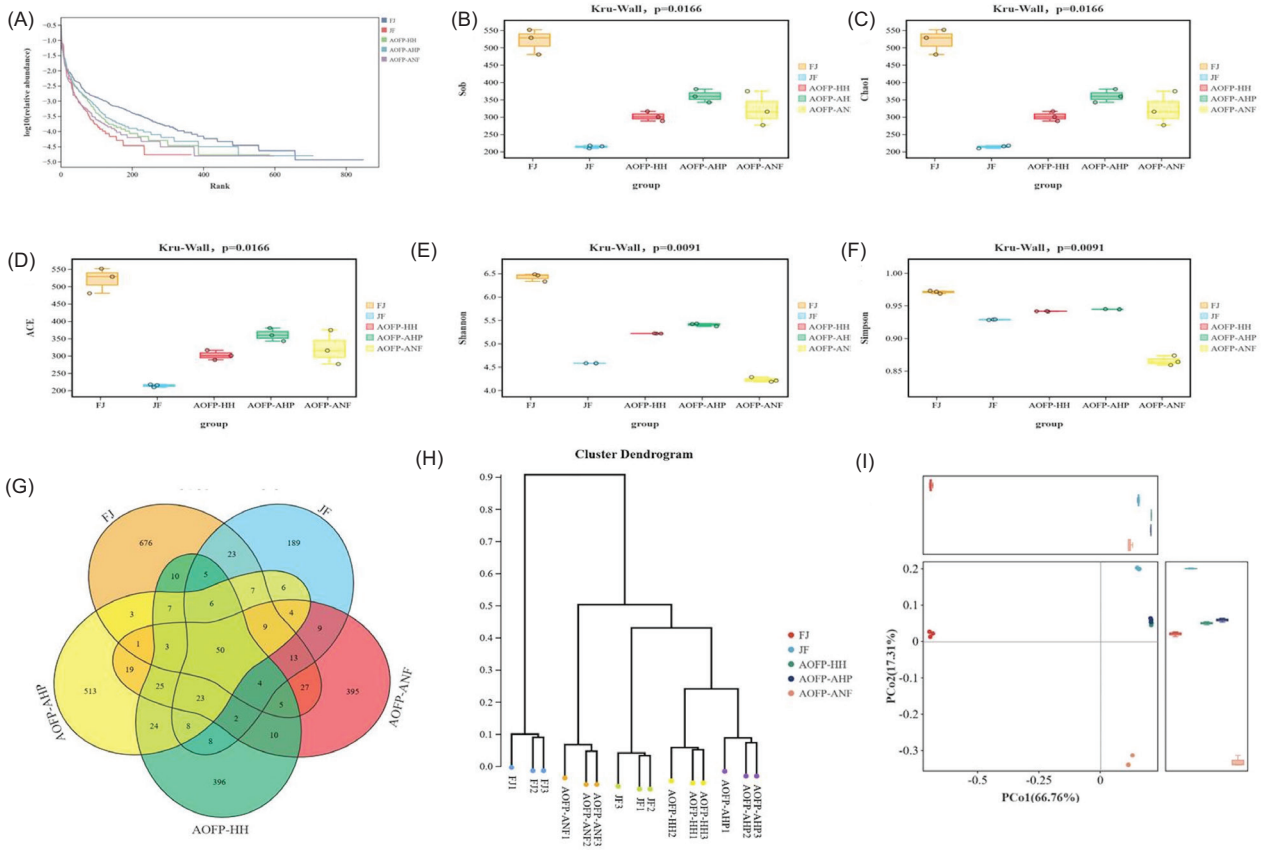

Figure 6. Analysis of microbial community diversity: (A-F) Alpha diversity indices; (G) Venn diagram of species distribution; (H & I) Beta diversity analysis.

among the five experimental groups (Kruskal–Wallis test, P = 0.0166). The FJ group exhibited the highest microbial diversity, with Shannon index (6.4 ± 0.2), Chao1 (536 ± 13), and ACE index (530 ± 12) all significantly surpassing other groups (P < 0.05). Its rank abundance curve showed a steep decline in low-rank regions, indicating a complex community structure with even species distribution. Conversely, the JF group displayed the lowest diversity levels, characterized by minimal Shannon (4.6 ± 0.3) and Simpson (0.93 ± 0.04) indices, while Chao1 and ACE indices were only 40% of FJ values (P < 0.01); its rank-abundance curve suggested dispersed dominant taxa. Notably, AOFP intervention groups demonstrated treatment-dependent patterns: The AOFP-HH group showed an intermediate Shannon index (5.3 ± 0.3) between FJ and JF, with a 58% higher Chao1 than JF (P < 0.05), but a plateau in low-rank regions of its rank-abundance curve implied convergence toward specific dominant species. The AOFP-AHP group paradoxically presented the highest Shannon index (5.5 ± 0.2) alongside the lowest Chao1 (360 ± 8), reflecting reduced richness concurrent with dominance concentration. The AOFP-ANF group exhibited the lowest Simpson index (0.86 ± 0.05) and Shannon index (4.2 ± 0.3) comparable to JF. Collectively, these findings indicate that AOFP interventions selectively enriched functionally core taxa, enhancing community functional stability despite reducing overall diversity, providing theoretical support for a "quality over quantity" strategy in microbiota modulation.

Beta diversity analysis

The beta diversity analysis compares the overall community structure between experimental and control groups by assessing species diversity. Based on Figures 6H and 6i, AOFP intervention significantly altered gut microbiota composition. Sample distances in the PCoA ordination reflect community similarity, with the FJ group forming a distinct branch and clearly separating from the JF group. The AOFP intervention group clustered tightly in the PCoA space, positioned in the positive direction of the PCo1 axis, indicating convergent community structure post-intervention.

Within-group clustering distances for the three AOFP subgroups were smaller than between-group differences, demonstrating that microbiota remodeling effect of AOFP outweighs intrinsic variability. PCo1 was positively correlated with Firmicutes abundance and negatively correlated with Bacteroidota. FJ group samples clustered in the negative PCo1 direction, exhibiting the highest Bacteroidota proportion and reflecting the native microbiota composition of the original fecal inoculum. On the other hand, JF group samples occupied the positive PCo1 direction with elevated Firmicutes abundance but displayed metabolic function dispersion along PCo2. Samples from AOFP-HH, AOFP-AHP, and AOFP-ANF formed tight clusters along the positive PCo1 axis, all with Firmicutes proportions exceeding 65% and convergent PCo2 values. This suggests AOFP intervention drives the community toward a stable, Firmicutes-dominated state. Collectively, PCoA and clustering analyses confirm that AOFP intervention induced community polarization, which enhanced functional stability through structural reshaping and metabolic convergence. The tight clustering of AOFP samples along the positive PCo1 axis highlights the stepwise regulatory influence of carbon source type and ratio on community composition. These findings provide a structural and biological foundation for precise gut microbiota modulation.

PCoA analysis of the AOFP-HH and AOFP-AHP groups showed convergence toward a Firmicutes-dominated state, suggesting that high-pressure treatment may selectively enrich specific genera by releasing digestion-resistant fragments. The unique enrichment of Fusobacteriota in the AOFP-ANF group suggests its potential immunomodulatory function. Fusobacterium can activate regulatory T cells (Tregs) through the TLR4/NF-κB pathway, secrete IL-10, and inhibit proinflammatory cytokines (Liu *et al*., 2025). The fermentation metabolites of AOFP-ANF may promote synergistic proliferation of Fusobacteriota with other microbiota through cross-feeding mechanisms, providing a new direction for developing polysaccharides with targeted immunomodulatory functions. The galacturonic acid in AOFP-HH binds to the intestinal mucus layer via hydrogen bonds, enhancing the physical barrier function (Ge *et al*., 2024). The low-molecular-weight fragments of AOFP-ANF are preferentially utilized by Bifidobacterium and Lactobacillus, promoting short-chain fatty acid synthesis (Lin *et al*., 2025). These results are consistent with Zhang *et al*.'s (2023) study on goji polysaccharides, where the structural complexity of polysaccharides determines the diversity of their metabolic pathways.

Functional prediction of gut microbiota

Based on Functional distribution overview (Figure 7), the three AOFP interventions significantly activated microbial functional profiles. The total abundance of metabolic pathways exceeded 400,000, accounting for 37.5–44.2% of the functional gene repertoire (significantly higher than the control group, $P < 0.05$). Carbohydrate metabolism was most enriched in the AOFP-HH (Figure 7A), suggesting that high-pressure and high-temperature extracted polysaccharides enhance carbohydrate decomposition via their well-ordered β-1,3-glucan structures. The AOFP-AHP group (Figure 7B) showed superior performance in cofactor and vitamin metabolism ($P < 0.01$), likely attributable to its low-molecular-weight fragments (1.03 kDa) promoting coenzyme synthesis (Cheng *et al*., 2024).

Within genetic information processing, the AOFP-ANF (Figure 7C) group exhibited the highest abundance of DNA replication or repair and translation functions ($P < 0.05$), supporting microbiota homeostasis through enhanced genomic stability and expression efficiency. For environmental adaptation, membrane transport activity in AOFP groups increased by 8.5% compared to the FJ group (AOFP-AHP > HH > ANF), with AOFP-AHP displaying the most active signal transduction ($P < 0.01$). This confirms that low-molecular-weight polysaccharides optimized adaptability by strengthening transmembrane transport and environmental responsiveness.

Functional remodeling demonstrated dose-dependent effects (Figure 7D): AOFP-HH dominated carbohydrate metabolism to drive butyrate synthesis; AOFP-AHP optimized membrane transport and coenzyme metabolism; AOFP-ANF showed weaker functional gains due to its molecular structural constraints (1.14 kDa).

Conclusion

This study systematically compared the effects of three extraction methods (high-pressure and high-temperature, HH; acid-assisted high-pressure and high-temperature, AHP; *A. niger* fermentation, ANF) on the structural characteristics, hypoglycemic activity, and gut microbiota modulation of AOFP. Our findings reveal a cascade regulatory mechanism linking extraction processes, structural features and bioactivities.

The HH method generated semicrystalline β-1,3-glucan chains (XRD peak at 32°) with folded lamellar structures (SEM), demonstrating superior hypoglycemic effects (97.08% α-amylase and 59.43% α-glucosidase inhibition). Mechanistically, the intact β-1,3-glycosidic bonds provided

a rigid scaffold that sterically hindered enzyme-substrate binding, while high galacturonic acid content (11.74%) enhanced hydrogen bonding, synergistically boosting inhibition. In contrast, AHP-derived AOFP showed disrupted glycosidic bonds, yielding amorphous low-MW fragments (1.03 kDa) with reduced activity (50.04% α-glucosidase inhibition). ANF-produced medium-MW polysaccharides (1.14 kDa) retained high α-amylase inhibition (95.5%) but exhibited weaker α-glucosidase inhibition (47%) due to random enzymatic cleavage.

We established a direct structure-activity relationship through conformational stability analysis. Congo red assays confirmed that AOFP-HH and AOFP-ANF maintained stable triple-helix structures under alkaline conditions, underpinning their bioactivity, whereas AOFP-AHP underwent conformational collapse due to hydrogen bond disruption. The semicrystalline state (XRD) and lamellar morphology (SEM) of HH-processed AOFP were identified as critical physical stabilizers.

All AOFPs variants shared core microbiota effects: early butyrate production doubled at 12 h, coupled with increased *Firmicutes* abundance (65.2% in HH group) and *Ligilactobacillus* proliferation (2.1-fold),

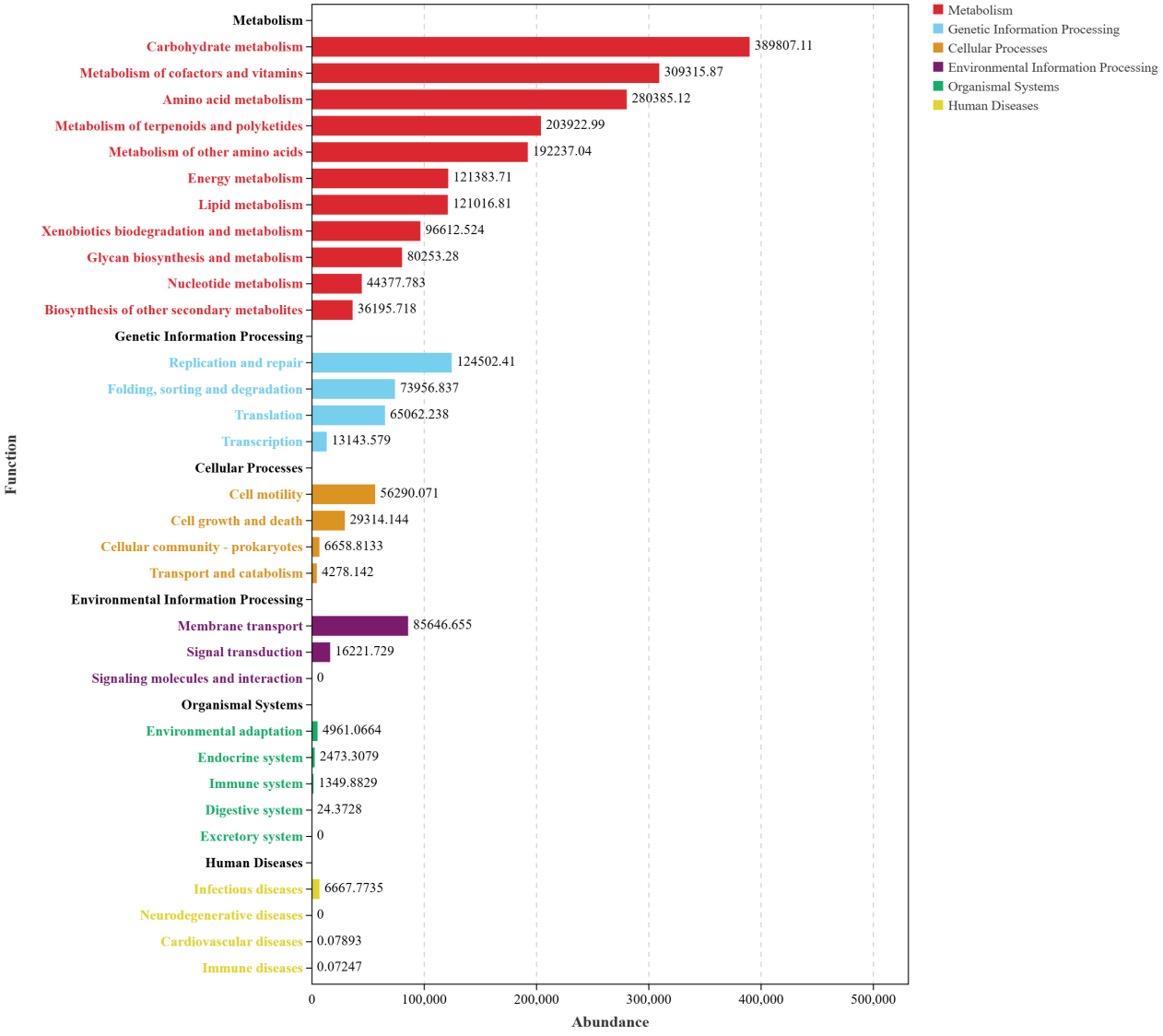

Figure 7. Functional distribution overview (A) Functional distribution overview diagram of AOFP-HH; (B) Functional distribution overview diagram of AOFP-AHP; (C) Functional distribution overview diagram of AOFP-ANF; (D) Stacked bar chart of functional abundance for AOFP-HH, AOFP-AHP, and AOFP-ANF.

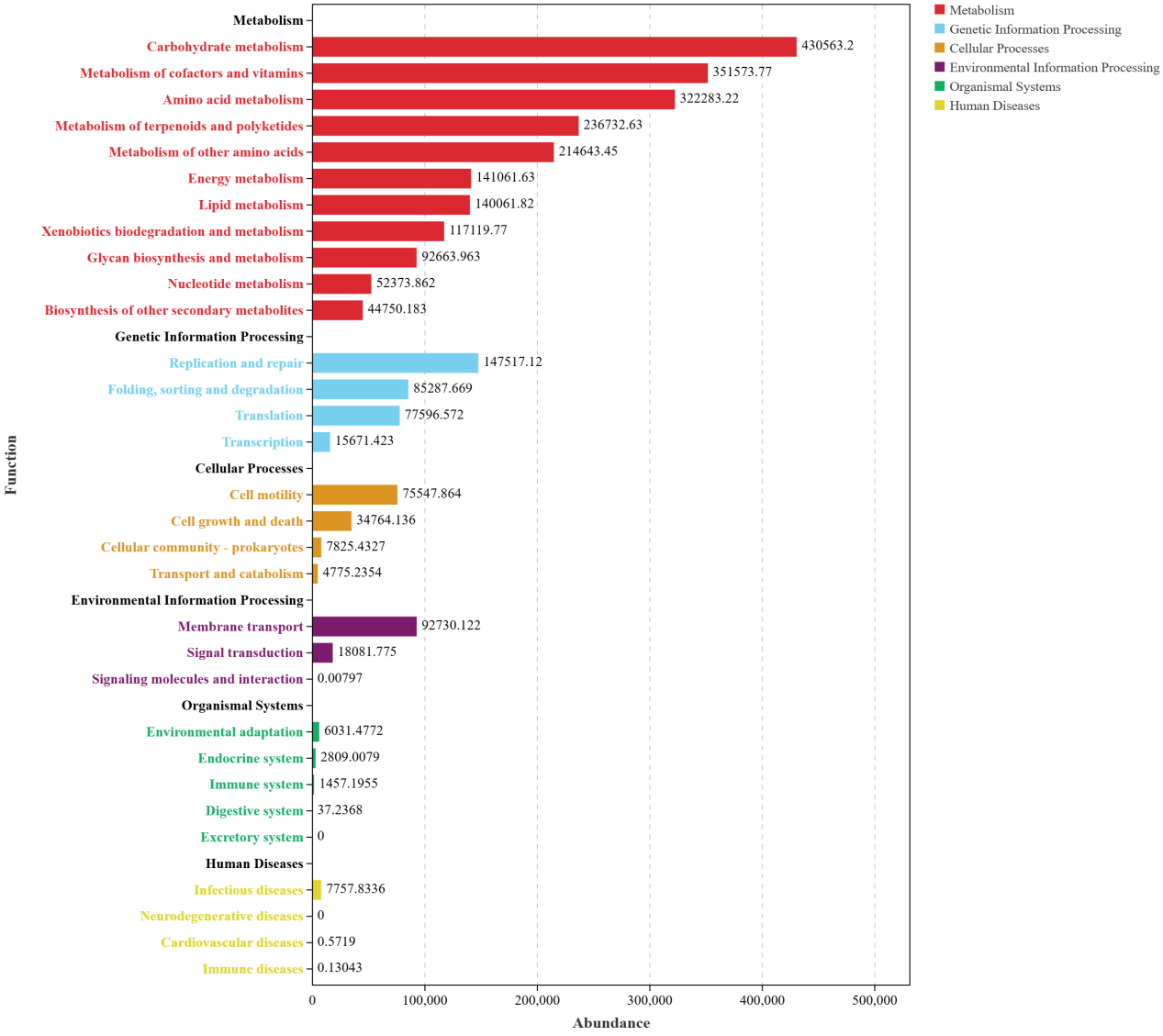

Figure 7 (Continued). Functional distribution overview (A) Functional distribution overview diagram of AOFP-HH; (B) Functional distribution overview diagram of AOFP-AHP; (C) Functional distribution overview diagram of AOFP-ANF; (D) Stacked bar chart of functional abundance for AOFP-HH, AOFP-AHP, and AOFP-ANF.

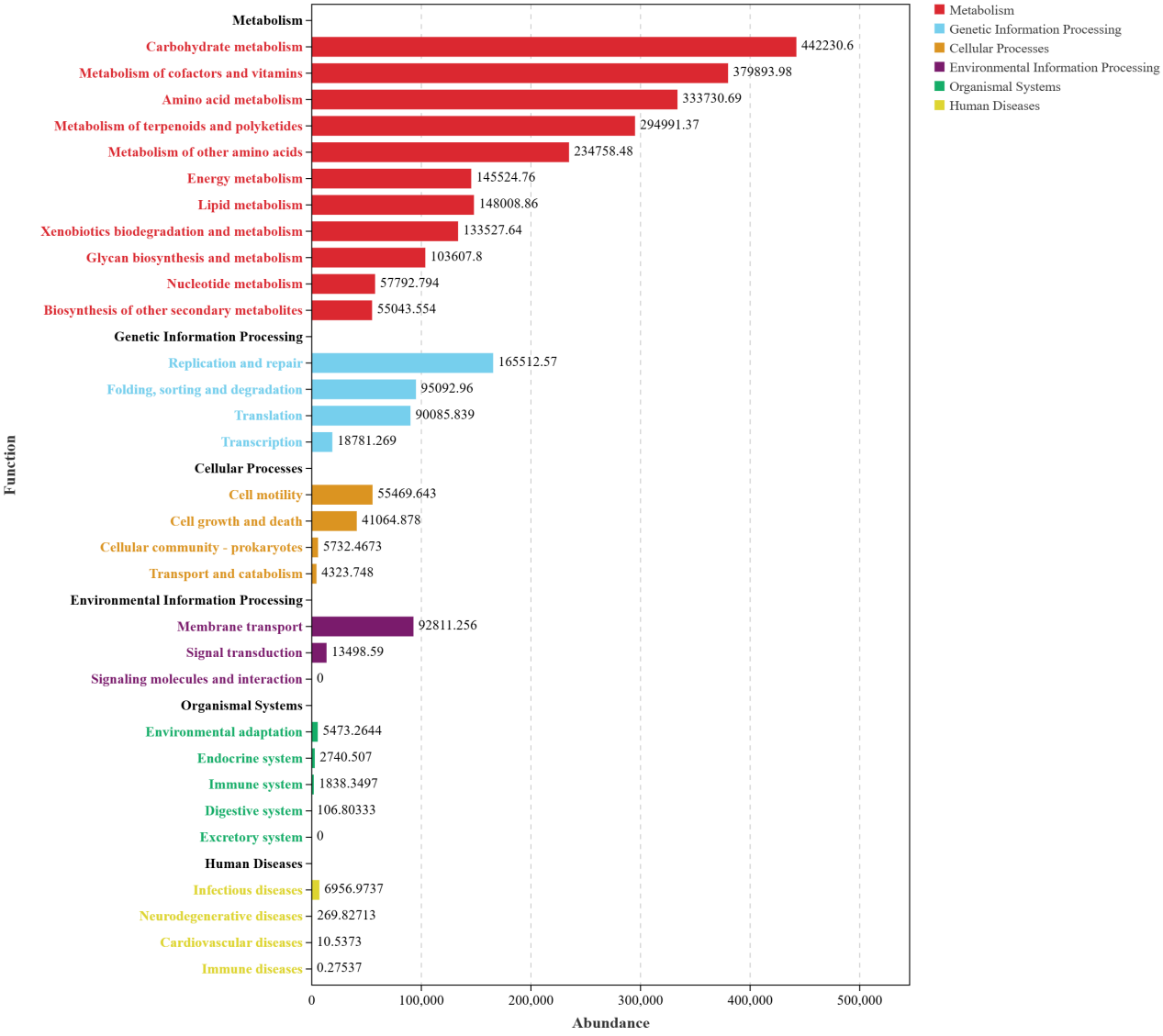

Figure 7 (Continued). Functional distribution overview (A) Functional distribution overview diagram of AOFP-HH; (B) Functional distribution overview diagram of AOFP-AHP; (C) Functional distribution overview diagram of AOFP-ANF; (D) Stacked bar chart of functional abundance for AOFP-HH, AOFP-AHP, and AOFP-ANF.

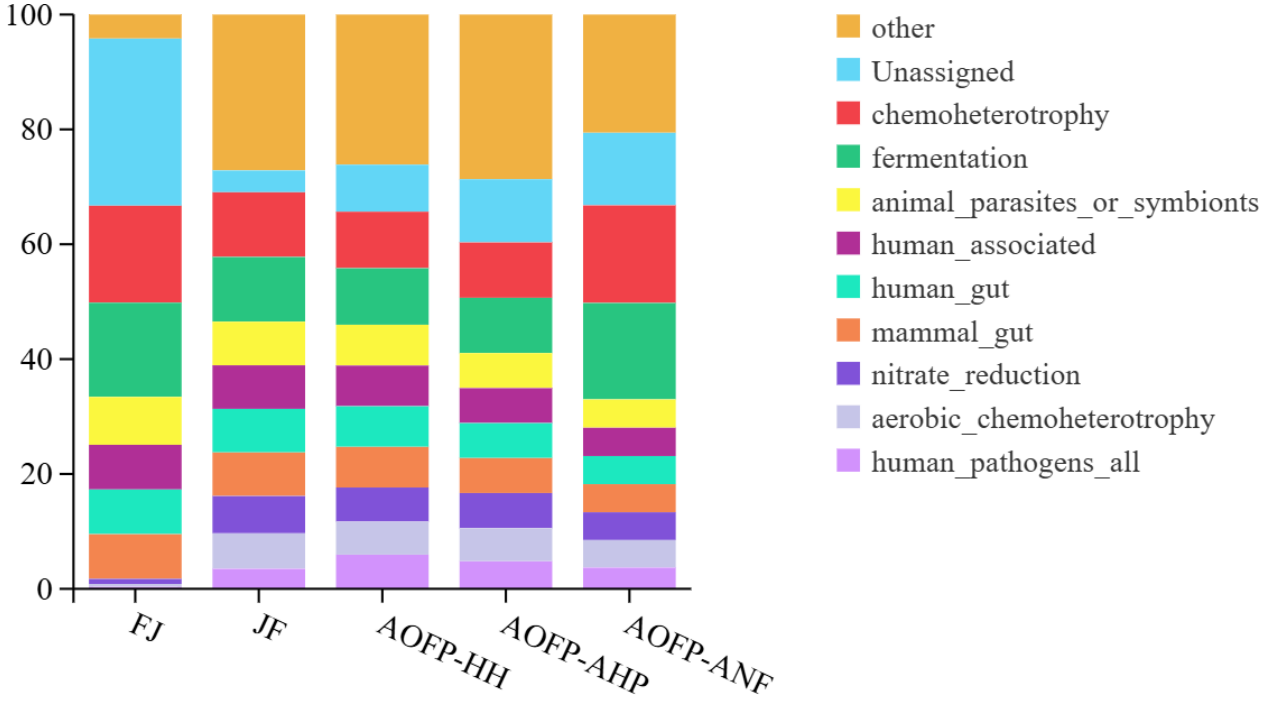

Figure 7 (Continued). Functional distribution overview (A) Functional distribution overview diagram of AOFP-HH; (B) Functional distribution overview diagram of AOFP-AHP; (C) Functional distribution overview diagram of AOFP-ANF; (D) Stacked bar chart of functional abundance for AOFP-HH, AOFP-AHP, and AOFP-ANF.

enhancing gut barrier function. Process-specific modulation was observed: HH/AHP groups converged toward *Firmicutes*-dominant communities (PCoA) and prioritized glycolytic pathways, establishing an "early butyrate/acetate" metabolic pattern. ANF uniquely enriched *Fusobacteriota* (predicted to modulate Th17/Treg balance) and completely metabolized arabinose while releasing mannose, suggesting cross-feeding-mediated microbial cooperation.

These results guide functional food development: AOFP-HH emerges as an ideal antidiabetic additive due to its high hypoglycemic activity, structural stability, and sustained butyrate production. AOFP-ANF's unique immunomodulatory potential (e.g., *Fusobacteriota* enrichment, mannose pathway activation) offers novel strategies for targeted probiotic formulations.

Mandatory Disclosure on Use of Artificial Intelligence

AI-assisted tools were used in the preparation of this manuscript. All references have been manually verified for accuracy and relevance.

Data Availability Declaration

All relevant data are included within the manuscript and its supporting information files.

Author Contributions

All authors contributed equally to this article.

Conflicts of Interest

The authors declare that they have no known competing financial interests or personal relationships that could have appeared to influence the work reported in this article.

Funding

This study was supported by grants from the Program for Scientific Research Start-Up Funds of Guangdong Ocean University (YJR24005); Guangdong TZ Plan Technology Entrepreneurship Leading Talent Project (2023TY07Y0290); The 2025 Provincial College Student Innovation and Entrepreneurship Training

Program Project (S202510566087); and the Science and Technology Planning Project in Guangdong, P.R. China (SDZX2022041, SDZX2023036 and SDZX2023033).

References

Borjigin, G., Wei, F., Jiang, S., Li, Q., Yang, C. 2023. Extraction, purification, structural characterization and biological activity of polysaccharides from Fritillaria: A review. International Journal of Biological Macromolecules. 242(2): 124817. https://doi.org/10.1016/j.ijbiomac.2023.124817

Cao, X.-Y., Liu, D., Bi, R.-C., He, Y. L., He, Y., Liu, J. L. 2019. The protective effects of a novel polysaccharide from Lentinus edodes mycelia on islet β (INS-1) cells damaged by glucose and its transportation mechanism with human serum albumin. International Journal of Biological Macromolecules. 134: 344–353. https://doi.org/10.1016/j.ijbiomac.2019.05.033

Chen, L., Liu, J., Ge, X., Xu, W., Chen, Y., Li, F., et al. 2019. Simulated digestion and fermentation in vitro by human gut microbiota of polysaccharides from Helicteres angustifolia L. International Journal of Biological Macromolecules. 141: 1065–1071. https://doi.org/10.1016/j.ijbiomac.2019.09.073

Cheng, C., Sun, M., Wang, L., Wang, H., Li, L., Yang, Q., et al. 2024. Zein and soy polysaccharide encapsulation enhances probiotic viability and modulates gut microbiota. LWT. 210: 116827. https://doi.org/10.1016/j.lwt.2024.116827

Chi, Y., Li, Y., Zhang, G., Gao, Y., Ye, H., Gao, J., et al. 2018. Effect of extraction techniques on properties of polysaccharides from Enteromorpha prolifera and their applicability in iron chelation. Carbohydrate Polymers. 181: 616–623. https://doi.org/10.1016/j.carbpol.2017.11.104

El-Gendi, H., Abu-Serie, M.M., Kamoun, E.A., Saleh, A.k., El-Fakharany, E.M. 2023. Statistical optimization and characterization of fucose-rich polysaccharides extracted from pumpkin (*Cucurbita maxima*) along with antioxidant and antiviral activities. International Journal of Biological Macromolecules. 232: 123372. https://doi.org/10.1016/j.ijbiomac.2023.123372

Ge, C.-C., Li, X.-Y., Qiao, W.-H., Cui, C., Wang, J., Gongpan, P., et al. 2024. BACE1 inhibitors from the fruits of *Alpinia oxyphylla* have efficacy to treat T2DM-related cognitive disorder. Fitoterapia. 178: 106157. https://doi.org/10.1016/j.fitote.2024.106157

Huang, K., Lin, M., Hsu, Y., Lu, I.H., Pan, I.H., Yang, J.L., et al. 2019. *Alpinia oxyphylla* fruit extract ameliorates experimental autoimmune encephalomyelitis through the regulation of Th1/Th17 Cells. Evidence-Based Complementary and Alternative Medicine. 2019: 6797030. https://doi.org/10.1155/2019/6797030

Jiang, L., Wang, W., Wen, P., Shen, M., Li, H., Ren, Y., et al. 2020. Two water-soluble polysaccharides from mung bean skin: Physicochemical characterization, antioxidant and antibacterial activities. Food Hydrocolloids. 100: 105412. https://doi.org/10.1016/j.foodhyd.2019.105412

Kačuráková, M., Capek, P., Sasinková, V., Wellner, N., Ebringerová, A. 2000. FT-IR study of plant cell wall model compounds: Pectic polysaccharides and hemicelluloses. Carbohydrate Polymers. 43(2): 195–203. https://doi.org/10.1016/S0144-8617(00)00151-X

Li, D., Zhu, G., Xu, Y., C., Ye, Y. J., Liu, J. M. 2020. Complete chloroplast genomes of three medicinal Alpinia species: Genome organization, comparative analyses and phylogenetic relationships in family Zingiberaceae. Plants (Basel). 9(2): 286. https://doi.org/10.3390/plants9020286

Li, H., Li, C., Xu, Y., Cao, H., Wang, X., He, J. 2025. Ultrasonic-assisted alkali extraction of quinoa polysaccharides: Yield and structural characterization. Journal of Cereal Science. 122: 104108. https://doi.org/10.1016/j.jcs.2025.104108

Li, X. and Wang, L., 2016. Effect of extraction method on structure and antioxidant activity of *Hohenbuehelia serotine* polysaccharides. International Journal of Biological Macromolecules. 83: 270–276. https://doi.org/10.1016/j.ijbiomac.2015.11.060

Li, Y., Zhou, X. and Fang, Z., 2024. Fang Zhaohui's clinical experience in treating diabetic nephropathy with Yizhiren (*Alpinia oxyphylla* seeds). Clinical Journal of Traditional Chinese Medicine. 36(7): 1256–1259. https://doi.org/10.16448/j.cjtcm.2024.0714

Liberato, M.V., Prates, E.T., Gonçalves, T.A., Bernardes, A., Vilela, N., Fattori, J., et al. 2021. Insights into the dual cleavage activity of the GH16 laminarinase enzyme class on β-1,3 and β-1,4 glycosidic bonds. Journal of Biological Chemistry. 296: 100385. https://doi.org/10.1016/j.jbc.2021.100385

Lin, Y., Wu, J., Xiong, B., Wang, L., Zeng, Z., Zheng, B., et al. 2025. Effect of digestive properties and gut microbiota structure of steam-exploded *Laminaria japonica* polysaccharide: In vitro dynamic human gastrointestinal systems. LWT. 225: 117866. https://doi.org/10.1016/j.lwt.2025.117866

Liu, C., Bai, J., Yang, S., Shi J, Qin Y, Wu D., et al. 2024. Optimization of acid extraction process for *Hovenia dulcis* polysaccharides and investigation of its physicochemical properties and antioxidant activities. Food and Fermentation Industries. 50(9): 148–156. https://doi.org/10.13995/j.cnki.11-1802/ts.035439

Liu, Z., Wang, M., Li, J., Zhao, Z., Wang, Z., Hu, Y., et al. 2025. Sulfated polysaccharide from *Hizikia fusiforme* selectively utilized by *Bacteroides caccae* and regulates its metabolite profile during in vitro fermentation. Food Bioscience. 69: 106816. https://doi.org/10.1016/j.fbio.2025.106816

Pan, L., Tu, Y., Li, Y., Wei, Z., Liu, L., Zhang, A., et al. 2025. Physicochemical analysis and hypoglycemic potential of *Tremella aurantialba* polysaccharides. Food and Fermentation Industries. 1–13. https://doi.org/10.13995/j.cnki.11-1802/ts.041529

Park, C.L., Kim, J.H., Jeon, J.S., Lee, J. H., Zhang, K., Guo, S., et al. 2022. Protective effect of *Alpinia oxyphylla* fruit against tert-butyl hydroperoxide-induced toxicity in HepG2 cells via Nrf2 activation and free radical scavenging and its active molecules. Antioxidants. 11: 1032. https://doi.org/10.3390/antiox11051032

Qian, J.-Y., Chen, W., Zhang, W.-M., Zhang, H. 2009. Adulteration identification of some fungal polysaccharides with SEM, XRD, IR and optical rotation: A primary approach. Carbohydrate Polymers. 78(3): 620–625. https://doi.org/10.1016/j.carbpol.2009.05.025

Ruan, X., 2021. Study on bioactive components of *Alpinia oxyphylla* from Guangxi and product development. Nanchang: Nanchang University. https://doi.org/10.27232/d.cnki.gnchu.2021.003672

Shang, H., Chen, S., Li, R., Zhou, H., Wu, H., Song, H. 2018. Influences of extraction methods on physicochemical characteristics and activities of *Astragalus cicer* L. polysaccharides. Process Biochemistry. 73: 220–227. https://doi.org/10.1016/j.procbio.2018.07.016

Shi, F., Yan, X., Cheong, K.-L., Liu, Y. 2018. Extraction, purification, and characterization of polysaccharides from marine algae *Gracilaria lemaneiformis* with anti-tumor activity. Process Biochemistry. 73: 197–203. https://doi.org/10.1016/j.procbio.2018.08.011

Shi, W., Zhong, J., Zhang, Q., Yan, C. 2020. Structural characterization and antineuroinflammatory activity of a novel heteropolysaccharide obtained from the fruits of *Alpinia oxyphylla*. Carbohydrate Polymers. 229: 115405. https://doi.org/10.1016/j.carbpol.2019.115405

Song, H., Zhang, Y., Huang, Q., Wang, F., Wang, L., Xiong, L., et al. 2025. Extraction optimization, purification, characterization, and hypolipidemic activities of polysaccharide from pumpkin. International Journal of Biological Macromolecules. 141907. https://doi.org/10.1016/j.ijbiomac.2025.141907

Song, J., Wu, Y., Ma, X., Feng, L., Wang, Z., Jiang, G., et al. 2020. Structural characterization and α-glycosidase inhibitory activity of a novel polysaccharide fraction from *Aconitum coreanum*. Carbohydrate Polymers. 230: 115586. https://doi.org/10.1016/j.carbpol.2019.115586

Sun, Y., Zeng, H., Huang, J., Zhao, Y., Cai, J., Sun, S., et al. 2025. Isolation, purification, structural characterization and in vitro hypolipidemic activity of Wuzhuyu polysaccharides. Science and Technology of Food Industry. 1–18 [2025-03-17]. https://doi.org/10.13386/j.issn1002-0306.2024070437

Tang, Y., Wei, Z., He, X., Ling, D., Qin, M., Yi, P., et al. 2024. A comparison study on polysaccharides extracted from banana flower using different methods: Physicochemical characterization, and antioxidant and antihyperglycemic activities. International Journal of Biological Macromolecules. 264(1): 130459. https://doi.org/10.1016/j.ijbiomac.2024.130459

Wang, L., Liu, H.-M. and Qin, G.-Y., 2017. Structure characterization and antioxidant activity of polysaccharides from Chinese quince seed meal. Food Chemistry. 234: 314–322. https://doi.org/10.1016/j.foodchem.2017.05.002

Wang, M., Hu, J., You, F., Ma, F., Peng, Y., Zhu, S., et al. 2025. Structural characteristics, in vitro activities, and gut microbiota regulatory mechanism of *Alpinia oxyphylla* oligosaccharides. Science and Technology of Food Industry. 1–17 [2025-10-24]. https://doi.org/10.13386/j.issn1002-0306.2025060074

Wang, R., Chen, P., Jia, F., Tang, J., Ma, F. 2012. Optimization of polysaccharides from *Panax japonicus* C.A. Meyer by RSM and its anti-oxidant activity. International Journal of Biological Macromolecules. 50(2): 331–336. https://doi.org/10.1016/j.ijbiomac.2011.12.023

Wang, X., Yan, H., Xu, Y., Li, D., Bao, Y., Dai, Z. 2024. Stability during colonic digestion and modulatory effects on fecal microbiota of different modified lutein nanoliposomes. Science and Technology of Food Industry. 45(16): 376–383. https://doi.org/10.13386/j.issn1002-0306.2023090276

Xiang, H., Wen, W., Xu, P., Qiu, H., Chu, C., Shao, Q., et al. 2024. Inhibition mechanism of α-glucosidase by three geranylated compounds: Kinetic, spectroscopic and molecular docking. Process Biochemistry. 136: 237–244. https://doi.org/10.1016/j.procbio.2023.11.034

Yang, W., Su, L., Wang, L., Wu, J., Chen, S. 2022. Alpha-glucanotransferase from the glycoside hydrolase family synthesizes α(1–6)-linked products from starch: Features and synthesis pathways of the products. Trends in Food Science & Technology. 128: 160–172. https://doi.org/10.1016/j.tifs.2022.08.001

Yang, X., 2020. Structural characteristics and immunomodulatory activity of polysaccharides from *Alpinia oxyphylla*. Haikou: Hainan University. https://doi.org/10.27073/d.cnki.ghadu.2020.001252

Yang, X., Zhou, S., Li, H., An, J., Li, C., Zhou, R., et al. 2021. Structural characterization of *Alpiniae oxyphyllaefructus* polysaccharide 2 and its activation effects on RAW264.7 macrophages. International Immunopharmacology. 97: 107708. https://doi.org/10.1016/j.intimp.2021.107708

Yin, D., Sun, X., Li, N., Guo, Y., Tian, Y., Wang, L. 2021. Structural properties and antioxidant activity of polysaccharides extracted from *Laminaria japonica* using various methods. Process Biochemistry. 111(2): 201–209. https://doi.org/10.1016/j.procbio.2021.10.019

Yin, Q., Xu, W., Wu, K., Meng, P., Cai, J., Lin, C. 2024. Effects of different extraction methods on physicochemical properties and bioactivities of polygonatum polysaccharides. Modern Food Science and Technology. 40(3): 142–152. https://doi.org/10.13982/j.mfst.1673-9078.2024.3.0112

Yusoff, M.H.M. and Shafie, M.H., 2024. A review of in vitro antioxidant and antidiabetic polysaccharides: Extraction methods, physicochemical and structure-activity relationships. International Journal of Biological Macromolecules. 282(4): 137143. https://doi.org/10.1016/j.ijbiomac.2024.137143

Zeng, D. and Zhu, S., 2018. Purification, characterization, antioxidant and anticancer activities of novel polysaccharides extracted from Bachu mushroom. International Journal of Biological Macromolecules. 107(A): 1086–1092. https://doi.org/10.1016/j.ijbiomac.2017.09.088

Zeng, W., 2022. Structural characterization, digestive properties and bioactivities of *Lycium barbarum* polysaccharides. Yinchuan: North Minzu University. https://doi.org/10.27754/d.cnki.gbfmz.2022.000333

Zhang, F., 2023. Adsorption, in vitro digestion, and gut microbiota fermentation properties of four *Poria cocos* polysaccharides. Hainan: Hainan University of Traditional Chinese Medicine. https://doi.org/10.27138/d.cnki.ghuzc.2023.000484

Zhang, M., Zhuang, H., Zhang, X., Wang, X., Fu, X., Chen,S., et al. 2025. Structural characteristics of areca nut seed neutral polysaccharide and its impact on gut microbiota from human feces. Food Hydrocolloids. 158: 110492. https://doi.org/10.1016/j.foodhyd.2024.110492

Zhang, Q., Cui, C., Chen, C.-Q., Hu, X.-L., Liu, Y.-H., Fan, Y.-H., et al. 2015. Anti-proliferative and pro-apoptotic activities of *Alpinia oxyphylla* on HepG2 cells through ROS-mediated signaling pathway. Journal of Ethnopharmacology. 169: 99–108. https://doi.org/10.1016/j.jep.2015.03.073

Zhang, Q., Zheng, Y., Hu, X., Hu, X., L, W., L, D., et al. 2018. Ethnopharmacological uses, phytochemistry, biological activities, and therapeutic applications of *Alpinia oxyphylla* Miquel: A review. Journal of Ethnopharmacology. 224: 149–168. https://doi.org/10.1016/j.jep.2018.05.002

Zhang, Y., Xing, H., Liu, H., Qiao, S. 2023. Extraction, purification and antioxidant activity analysis of *Sophora japonica* polysaccharides. Science and Food Industry. 44(24): 207–215. https://doi.org/10.13386/j.issn1002-0306.2023020274

Zhao, Z., Wang, L., Ruan, Y., Wen, C., Ge, M., Qian, Y., et al. 2023. Physicochemical properties and biological activities of polysaccharides from the peel of *Dioscorea opposite* Thunb. extracted by four different methods. Food Science and Human Wellness. 12(1): 130–139. https://doi.org/10.1016/j.fshw.2022.07.031

Zheng, M., Ouyang, H., Li, Z., Hong, T., Zhu, Y., Yang, Y., et al. 2024. Ultra-high pressure assisted extraction of polysaccharide from *Bangia fusco-purpurea*: Structure and in vitro hypolipidemic activity. International Journal of Biological Macromolecules. 280(4): 135687. https://doi.org/10.1016/j.ijbiomac.2024.135687

Zheng, W., Yang, L., Meng, Y., Yang, L., Wu, J. 2024. Enhancing the catalytic efficiency of nitrilase for sterically hindered substrates by distal sites engineering. Green Synthesis and Catalysis. 110492. https://doi.org/10.1016/j.gresc.2024.11.002